The Remarkable Similarity of Massive Galaxy Clusters from z ~ 0 to z ~ 1.9

The Astrophysical Journal, 843:28 (15pp), 2017 July 1 https://doi.org/10.3847/1538-4357/aa7740

The Remarkable Similarity of Massive Galaxy Clusters from $z \sim 0$ to $z \sim 1.9$

M. McDonald[1], S. W. Allen[2,3,4], M. Bayliss[1], B. A. Benson[5,6,7], L. E. Bleem[6,7,8], M. Brodwin[9], E. Bulbul[1], J. E. Carlstrom[6,7,8,10], W. R. Forman[11], J. Hlavacek-Larrondo[12], G. P. Garmire[13], M. Gaspari[14,15], M. D. Gladders[6,7], A. B. Mantz[2,3,4], and S. S. Murray[11]
[1] Kavli Institute for Astrophysics and Space Research, Massachusetts Institute of Technology, 77 Massachusetts Avenue, Cambridge, MA 02139, USA
mcdonald@space.mit.edu
[2] Kavli Institute for Particle Astrophysics and Cosmology, Stanford University, 452 Lomita Mall, Stanford, CA 94305, USA
[3] Department of Physics, Stanford University, 382 Via Pueblo Mall, Stanford, CA 94305, USA
[4] SLAC National Accelerator Laboratory, 2575 Sand Hill Road, Menlo Park, CA 94025, USA
[5] Fermi National Accelerator Laboratory, Batavia, IL 60510-0500, USA
[6] Kavli Institute for Cosmological Physics, University of Chicago, Chicago, IL 60637, USA
[7] Department of Astronomy and Astrophysics, University of Chicago, Chicago, IL 60637, USA
[8] Argonne National Laboratory, 9700 S. Cass Avenue, Argonne, IL 60439, USA
[9] Department of Physics and Astronomy, University of Missouri, 5110 Rockhill Road, Kansas City, MO 64110, USA
[10] Department of Physics, University of Chicago, 5640 South Ellis Avenue, Chicago, IL 60637, USA
[11] Harvard-Smithsonian Center for Astrophysics, 60 Garden Street, Cambridge, MA 02138, USA
[12] Département de Physique, Université de Montréal, C.P. 6128, Succ. Centre-Ville, Montréal, Québec H3C 3J7, Canada
[13] Huntingdon Institute for X-ray Astronomy, LLC, USA
[14] Department of Astrophysical Sciences, Princeton University, Princeton, NJ 08544, USA
Received 2017 February 16; revised 2017 May 22; accepted 2017 June 1; published 2017 June 28

Abstract

We present the results of a *Chandra* X-ray survey of the eight most massive galaxy clusters at $z > 1.2$ in the South Pole Telescope 2500 deg^2 survey. We combine this sample with previously published *Chandra* observations of 49 massive X-ray-selected clusters at $0 < z < 0.1$ and 90 Sunyaev–Zel'dovich–selected clusters at $0.25 < z < 1.2$ to constrain the evolution of the intracluster medium (ICM) over the past ∼10 Gyr. We find that the bulk of the ICM has evolved self-similarly over the full redshift range probed here, with the ICM density at $r > 0.2R_{500}$ scaling like $E(z)^2$. In the centers of clusters ($r \lesssim 0.01R_{500}$), we find significant deviations from self-similarity ($n_e \propto E(z)^{0.2\pm0.5}$), consistent with no redshift dependence. When we isolate clusters with overdense cores (i.e., cool cores), we find that the average overdensity profile has not evolved with redshift—that is, cool cores have not changed in size, density, or total mass over the past ∼9–10 Gyr. We show that the evolving "cuspiness" of clusters in the X-ray, reported by several previous studies, can be understood in the context of a cool core with fixed properties embedded in a self-similarly evolving cluster. We find no measurable evolution in the X-ray morphology of massive clusters, seemingly in tension with the rapidly rising (with redshift) rate of major mergers predicted by cosmological simulations. We show that these two results can be brought into agreement if we assume that the relaxation time after a merger is proportional to the crossing time, since the latter is proportional to $H(z)^{-1}$.

Key words: galaxies: clusters: general – galaxies: clusters: intracluster medium – galaxies: high-redshift – X-rays: galaxies: clusters

1. Introduction

As the most massive collapsed structures in the universe, galaxy clusters provide unique laboratories for studying physics on very large and energetic scales. In particular, X-ray observations of galaxy clusters, which probe the hot ($\gtrsim 10^7$ K) intracluster medium (ICM), lead to an understanding of cluster-cluster mergers, the most energetic phenomena in the universe (e.g., Markevitch et al. 2002; Sarazin 2002); allow detailed studies of the effects of active galactic nuclei (AGNs) on large scales (see reviews by Fabian 2012; McNamara & Nulsen 2012); and provide some of the tightest constraints on the amount and distribution of matter in our universe (e.g., Mantz et al. 2010; de Haan et al. 2016). The cores of galaxy clusters represent one of the least understood regimes outside of our galaxy (see review by Kravtsov & Borgani 2012), with runaway cooling of the hot ICM (e.g., Fabian 1994; McDonald et al. 2012) seemingly being held in check by frequent outbursts of AGN feedback (e.g., Rafferty et al. 2008; Hlavacek-Larrondo et al. 2015)—a phenomenon that simulations are only recently beginning to reproduce (e.g., Gaspari et al. 2011, 2017; Prasad et al. 2015).

While the detailed physics of the ICM in nearby clusters has been studied in depth, the evolution of the ICM has only recently become an active area of research. This change is due, in large part, to the success of Sunyaev–Zel'dovich (SZ; Sunyaev & Zeldovich 1972) surveys, which select galaxy clusters via their imprint on the cosmic microwave background (CMB)—an effect that is, in principle, independent of redshift. Since the first discovery of a galaxy cluster via the SZ effect (Staniszewski et al. 2009), the number of new, distant, SZ-selected galaxy clusters has, on average, more than doubled every year (Vanderlinde et al. 2010; Marriage et al. 2011; Planck Collaboration et al. 2011; Hasselfield et al. 2013; Reichardt et al. 2013; Planck Collaboration et al. 2014; Bleem et al. 2015; Planck Collaboration et al. 2015). At the same time, optical and near-infrared (NIR) selection (based on galaxy overdensity) has matured, yielding complementary stellar mass–selected galaxy cluster catalogs over redshift ranges similar to those of the SZ surveys (e.g., Eisenhardt et al. 2008; Muzzin et al. 2009; Brodwin et al. 2013; Rettura et al. 2014; Stanford et al. 2014).

[15] Einstein and Spitzer Fellow.

With the rapid growth of NIR- and SZ-selected cluster catalogs has come the ability to study galaxy cluster evolution over an unprecedented range in redshift. However, the majority of the X-ray follow-up of the most distant clusters has focused on single extreme objects, such as XMMXCS J2215.9–1738 at $z = 1.46$ (Hilton et al. 2010), XDCP J0044.0-2033 at $z = 1.579$ (Tozzi et al. 2015), IDCS J1426.5+3508 at $z = 1.75$ (Brodwin et al. 2016), and 3C294 at $z = 1.786$ (Fabian et al. 2003). This relative lack of statistically complete X-ray studies of distant clusters, with few exceptions (e.g., Fassbender et al. 2011), is broadly due to the small number of known high-z clusters and the increased exposure times necessary at such high redshifts. Without such samples, our ability to make general conclusions about cluster evolution is severely limited.

In recent years, we have completed a survey of 90 SZ-selected clusters with the *Chandra X-ray Observatory*, spanning $0.25 < z < 1.2$ and with $M_{500} \gtrsim 3 \times 10^{14}\,M_{\odot}$. These clusters were drawn from the South Pole Telescope (SPT) 2500 deg^2 survey (Bleem et al. 2015) and observed to uniform depth with *Chandra* from 2011 to 2014. These data have advanced our understanding of the evolution of the ICM substantially, allowing detailed evolutionary studies of ICM cooling in cluster cores (Semler et al. 2012; McDonald et al. 2013), average entropy and pressure profiles (McDonald et al. 2014), AGN feedback (Hlavacek-Larrondo et al. 2015), ICM metallicity (McDonald et al. 2016), and ICM morphology (Nurgaliev et al. 2017) while also providing tight constraints on the amount and distribution of matter in the universe (Bocquet et al. 2015; Chiu et al. 2016; de Haan et al. 2016). These studies benefit from the unique combination of the SPT selection function, which is roughly independent of both redshift (e.g., Bleem et al. 2015) and the dynamical state of the cluster (e.g., Nurgaliev et al. 2017; Sifón et al. 2016), and uniform-depth *Chandra* follow-up, meaning that each cluster was observed for sufficient time to collect ∼1500–2000 X-ray photons. The latter allows a consistent analysis over the full redshift range of the sample, free from any biases that are signal-to-noise dependent.

Here, we extend those previous studies by including new *Chandra* observations of a mass-selected sample of eight SPT-selected clusters at $1.2 < z < 1.9$. This represents the first X-ray analysis of a mass-complete cluster sample at $z > 1.2$, providing new constraints on the thermodynamic state of massive galaxy clusters only ∼1–2 Gyr after their collapse. This epoch is roughly the peak of both star formation (see review by Madau & Dickinson 2014) and AGN activity (e.g., Wolf et al. 2003), two processes that can alter the chemical and thermodynamic state of the ICM, respectively. In this work, we focus specifically on properties determined from the X-ray surface brightness, deferring detailed spectroscopic analysis to a future paper. In Section 2, we describe the data used in this paper, including the low-z cluster sample from Vikhlinin et al. (2009) and intermediate-z sample from McDonald et al. (2013). In Section 3, we discuss our main results, focusing on ICM density profiles and the X-ray morphology of high-z clusters. In Section 4, we place these results in the context of previous works and state-of-the-art simulations, and we provide a summary and look toward the future in Section 5.

Throughout this work, we assume ΛCDM cosmology with $H_0 = 70\,\mathrm{km\,s^{-1}\,Mpc^{-1}}$, $\Omega_M = 0.3$, and $\Omega_\Lambda = 0.7$ and define M_{500} and R_{500} in terms of the critical density: $M_{500} \equiv \frac{4\pi}{3} 500 \rho_{\rm crit}(z) R_{500}^3$.

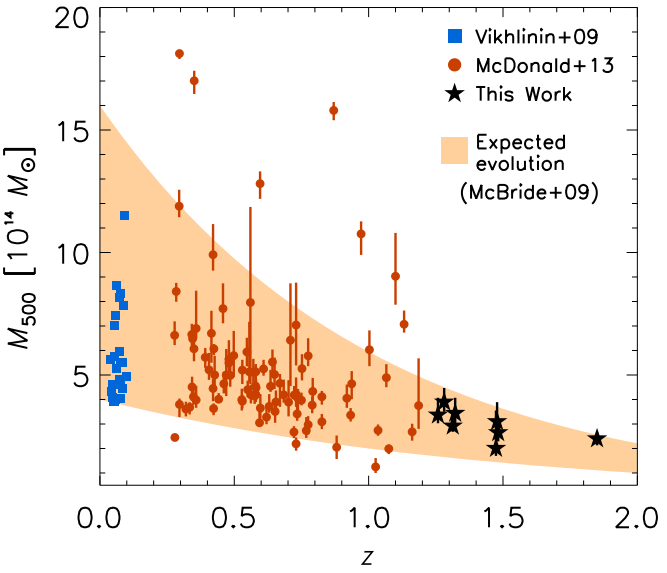

Figure 1. Mass vs. redshift for the three cluster samples described in Section 2.1. The black stars represent the new clusters presented in this work, while the red circles and blue squares show data from McDonald et al. (2013) and Vikhlinin et al. (2009), respectively. The tan shaded region shows the expected growth track for clusters with $M_{500} \sim 2$–$3 \times 10^{14}\,M_{\odot}$ at $z \sim 1.5$ from McBride et al. (2009). This demonstrates that the clusters we are observing at $z > 1.2$ are the progenitors of the intermediate- and low-z samples to which we compare.

2. Data and Analysis

2.1. Samples

In this work, we attempt to trace the evolution of clusters from $z \sim 0$ to $z \sim 1.9$. This is done by combining the low-z X-ray-selected sample from Vikhlinin et al. (2009) with SPT-selected samples at intermediate (McDonald et al. 2013) and high z. Where appropriate, we apply a mass cut to the X-ray samples to ensure a clean comparison across all redshifts, as shown in Figure 1. Below, we discuss the specific details of each data set, including the origin, availability, and quality of X-ray data.

2.1.1. SPT-Hiz: $1.2 < z < 1.9$

The high-z sample, referred to hereafter as "SPT-Hiz," consists of the eight most massive galaxy clusters at $z > 1.2$ in the 2500 deg^2 SPT-SZ survey (Bleem et al. 2015). These clusters have $2 \times 10^{14}\,M_{\odot} < M_{500} < 4 \times 10^{14}\,M_{\odot}$ and $1.2 < z < 1.9$, as shown in Figure 1. *Chandra* observations were obtained for each of these clusters as part of a Cycle 16 Large Program (PI: McDonald). For each cluster, we aimed for a total of 1500 counts, where the expected luminosity was derived from the SZ signal assuming the ξ–M (Bleem et al. 2015) and M–L_X (Vikhlinin et al. 2009) relations. This number of counts has been demonstrated to yield reliable single-temperature and metallicity estimates (McDonald et al. 2016), allow the measurement of the gas density out to $\sim R_{500}$ (McDonald et al. 2013), and determine accurate X-ray morphologies (Nurgaliev et al. 2013, 2017).

Spectroscopic redshifts for most of these clusters are derived based on Low Dispersion Survey Spectrograph (LDSS3; Allington-Smith et al. 1994) spectroscopy of ∼5–10 member galaxies per cluster (L. E. Bleem et al. 2017, in preparation), with three exceptions. SPT-CLJ0205-5829 and SPT-CLJ2040-4451, among the earliest clusters confirmed, have optical spectroscopy presented

in Stalder et al. (2013) and Bayliss et al. (2014), respectively. SPT-CLJ0459-4947 was not detected in our deep spectroscopic follow-up campaign. However, we have deep *Hubble Space Telescope* (*HST*) imaging of this cluster with Wide Field Camera 3-Ultraviolet (WFC3-UVIS) and Wide Field Camera 3-Infrared (WFC3-IR) that reveals a rich red sequence, allowing us to measure a photometric redshift (V. Strazzullo et al. 2017, in preparation). We also have independent redshift constraints for this system from *Spitzer* photometry and from a spectroscopic analysis of the *Chandra* data presented here. Independently, we measure $z = 1.85$, $z = 1.84$, and $z > 1.5$ from the *HST*, *Chandra*, and *Spitzer* data for SPT-CLJ0459-4947. We adopt a redshift of 1.85 for this system but stress that the accuracy is at the $\Delta z \sim 0.1$ level. Given that the majority of the analysis presented here requires us to bin all eight systems at $z > 1.2$ into a single average system, the precise redshift of this single system is relatively unimportant.

2.1.2. SPT-XVP: $0.25 < z < 1.2$

We include in this analysis a sample of 90 galaxy clusters spanning $0.25 < z < 1.2$, which has been referred to as the "SPT-XVP" sample in previous works (McDonald et al. 2013, 2014). The bulk of these clusters were observed by *Chandra* via an X-ray visionary program (hence the name) to obtain shallow X-ray imaging of the 80 most massive SPT-selected clusters at $z > 0.3$ (PI: Benson). Additional *Chandra* observations were obtained through various smaller Guest Observer (GO; PIs: McDonald, Mohr) and Guaranteed Time Observer (GTO; PIs: Garmire, Murray) programs or were already available in the archive. For the most part, these observations are of similar depth, with ∼2000 X-ray counts per cluster (see Figure 2 in McDonald et al. 2014). Details of these clusters (selection, masses, redshifts, and positions) are provided in Bleem et al. (2015), while additional information about the X-ray follow-up can be found in McDonald et al. (2013, 2014). With few exceptions, clusters are selected for X-ray follow-up by mass, with the ∼20% most massive clusters in the full SPT-SZ survey having *Chandra* X-ray observations. The masses and redshifts of these clusters are shown in Figure 1. We exclude from any surface brightness profile analysis the seven highest rarity clusters (outliers from the shaded region), which may bias any stacked density profile.

2.1.3. Low-Redshift Clusters: $0.0 < z < 0.1$

For a low-redshift comparison, we use the sample of 49 X-ray-selected clusters from Vikhlinin et al. (2009). This sample was chosen due to the similarity between our X-ray analysis pipeline and that used in Vikhlinin et al. (2009; the former was modeled after the latter). We direct the reader to Voevodkin & Vikhlinin (2004) and Vikhlinin et al. (2009) for a detailed discussion of how these clusters were selected. In short, the sample is X-ray flux-limited and constrained in redshift to the range $0.025 < z < 0.1$. The fraction of merging clusters (defined by eye) in this sample ($31\% \pm 8\%$; Vikhlinin et al. 2009) is similar to that in the REXCESS sample ($39\% \pm 12\%$; Pratt et al. 2009) and the SPT-XVP sample ($20^{+7}_{-4}\%$; Nurgaliev et al. 2017). Each cluster in this low-z sample has deep *Chandra* data from which we have gas density and temperature profiles from Vikhlinin et al. (2009). From this sample, we only consider clusters with $M_{500} > 4 \times 10^{14}\, M_{\odot}$, in order to allow a fair comparison to the high-z SZ-selected clusters (see Figure 1). This yields a sample of 27 X-ray-selected clusters with masses spanning $4\, M_{\odot} \times 10^{14} < M_{500} < 1.2 \times 10^{15}\, M_{\odot}$. Assuming realistic evolution scenarios for massive halos (McBride et al. 2009), the clusters in the SPT-Hiz sample, which have typical masses of $2\text{–}3 \times 10^{14}\, M_{\odot}$, will ultimately end up having $M_{500} > 4 \times 10^{14}\, M_{\odot}$ at $z \sim 0$.

2.2. X-Ray Data Reduction

The analysis pipeline used in this analysis was adapted from Vikhlinin et al. (2006) and Andersson et al. (2011) and is described in detail in McDonald et al. (2013, 2014). We repeat the relevant aspects here but direct readers to any of the aforementioned references for additional details.

All *Chandra* data for the SPT-XVP and SPT-Hiz samples were reduced using CIAO version 4.7 and CALDB version 4.7.1. Exposures were initially filtered for flares before applying the latest calibrations and determining the appropriate blank-sky background (epoch-based). Due to the small angular size of distant clusters, we were able to use off-source regions on the Advanced CCD Imaging Spectrometer (ACIS-I) chip opposite the cluster to model the astrophysical background for each observation. In general, these regions were $>3R_{500}$ from the cluster center. The blank-sky background spectra were rescaled based on the observed 9.5–12.0 keV flux and combined with off-source regions to constrain the instrumental, particle, and astrophysical backgrounds. Point sources were identified and masked via an automated wavelet decomposition technique described in Vikhlinin et al. (1998). Cluster centers were chosen in two different ways, which we will consider throughout the text. The "peak" center was found by heavily binning and smoothing the image on ∼12″ scales and then measuring the centroid within 50 kpc of the peak (to allow subpixel accuracy). The "centroid" center was found by measuring the centroid within a 250–500 kpc aperture, following McDonald et al. (2013). This definition is less sensitive to core structure (e.g., sloshing) and is a better probe of the center of the large-scale dark matter potential. Unless otherwise noted, all measurements shown are with respect to the centroid center.

2.3. X-Ray Measurements

In this work, we focus on measurements derived from the X-ray surface brightness, deferring any spectroscopic analysis (aside from the metallicity evolution study already published by McDonald et al. 2016) to a future paper. For each cluster, we measure gas density profiles following Vikhlinin et al. (2006), Andersson et al. (2011), and McDonald et al. (2013) and X-ray morphology following Nurgaliev et al. (2013, 2017). Below, we briefly describe the relevant features of these analyses.

2.3.1. Gas Density Profiles

The surface brightness profile for each cluster is extracted in the energy range 0.7–2.0 keV in 20 annuli, defined as follows:

$$r_{\mathrm{out},i} = (a + bi + ci^2 + di^3) R_{500}\ i = 1 \ldots 20, \quad (1)$$

where $(a, b, c, d) = (13.779, -8.8148, 7.2829, -0.15633) \times 10^{-3}$ and R_{500} is initially estimated based on the M–T_X relation (see Andersson et al. 2011). This binning scheme is chosen to ensure that the profile is well sampled from core to outskirts and that the innermost bin is always resolved (>1 ACIS-I pixel in

radius) for clusters at all redshifts. For the cluster with the smallest angular size in our sample (SPT-CLJ0459-4947; $z = 1.85$, $R_{500} = 494$ kpc), the innermost bin has $r_{\rm out} = 0.''7$, corresponding to ~1.5 *Chandra* ACIS-I pixels in radius, or ~3 pixels in diameter. For all pointings, the cluster center is within $1'$ of the on-axis position, meaning that the innermost bin is roughly the size of or larger than the point spread function. Following Vikhlinin et al. (2006), we correct the surface brightness profiles for spatial variations in temperature, metallicity, and telescope effective area, assuming a universal temperature profile from Vikhlinin et al. (2006) normalized to the measured kT_{500} and a constant metallicity profile. Calibrated (including k-corrected) surface brightness profiles are expressed as an emission measure integral, $\int n_e n_p dl$, where n_e and n_p are the electron and proton densities, respectively. To deproject this into a three-dimensional electron density, we model the calibrated surface brightness profile with a modified β-model,

$$n_e n_p = n_0^2 \frac{(r/r_c)^{-\alpha}}{(1 + r^2/r_c^2)^{3\beta-\alpha/2}} \frac{1}{(1 + r^3/r_s^3)^{\epsilon/3}}, \quad (2)$$

which is projected along the line of sight through the full cluster volume to match the aforementioned emission measure integral. Here, n_0 is the density normalization and r_c and r_s are the scaling radii of the core and extended components, respectively. We estimate the three-dimensional gas density assuming $n_e = Zn_p$ and $\rho_g = m_p n_e A/Z$, where $A = 1.397$ and $Z = 1.199$ are the average nuclear charge and mass, respectively, for a plasma with $0.3\,Z_\odot$ metallicity. This assumption of constant, unevolving metallicity is well motivated by recent work (McDonald et al. 2016).

Gas masses are derived by integrating $\rho_g(r)$ over the cluster volume. We refine our estimate of M_{500} and R_{500} for each cluster by iteratively satisfying the $M_{\rm gas}$–M_{500} relation from Vikhlinin et al. (2009).

2.3.2. Morphology

Following Nurgaliev et al. (2013, 2017), we quantify the X-ray morphology using the "photon asymmetry" ($a_{\rm phot}$) statistic. This statistic quantifies the amount of asymmetry by comparing the cumulative distribution of X-ray counts as a function of azimuth for a given radial annulus to a uniform distribution, computing a probability that these two distributions are different. Combining these probabilities for multiple radial bins provides an overall probability that the cluster has azimuthally uniform brightness. This statistic, which is sensitive to azimuthal asymmetry, is complementary to statistics that measure the surface brightness concentration (e.g., Vikhlinin et al. 2007; Santos et al. 2008). Importantly, this statistic was shown to be unbiased to the quality of the data used in terms of both angular resolution and signal-to-noise ratio (Nurgaliev et al. 2013). This makes it optimal for comparing the morphology of clusters at low and high redshift, where both angular resolution and data quality can vary dramatically.

For each cluster, we measure $a_{\rm phot}$ with reference to both the peak and centroid centers (see Section 2.2). We report these measurements in Table 1 for the SPT-Hiz clusters; those for the SPT-XVP clusters are reported in Nurgaliev et al. (2017). We do not directly compare morphological measurements of high-z clusters to low-z, X-ray-selected clusters due to a lack of existing $a_{\rm phot}$ measurements for the latter.

3. Results

3.1. Gas Density Profiles

In McDonald et al. (2013), we demonstrated qualitatively that the gas density (ρ_g) profiles of massive clusters evolve self-similarly outside of $\sim 0.15R_{500}$ over the redshift range $0 < z < 1.2$. In the cores of clusters, this earlier work showed that the "peakiness" decreased significantly with increasing redshift, leading to less-cuspy density profiles at early times. In Figure 2, we extend this earlier analysis to include the eight SPT-Hiz clusters presented in this work. In the upper left panel of Figure 2, we show the gas density profiles for each of the SPT-Hiz clusters normalized to the critical density of the universe ($\rho_{\rm crit} \equiv 3H^2/8\pi G$) and in terms of the scaled radius, r/R_{500}. These profiles show an order of magnitude scatter in the innermost bin ($r \sim 0.01R_{500}$) and collapse onto a single profile by $r \sim 0.3R_{500}$. At large radii, the increased scatter is due to increased noise in the measurements, rather than real, physical scatter as observed in the cores. Next to these individual clusters, we show the average profile in five different redshift bins spanning $0 < z < 1.9$. As in McDonald et al. (2013), we see a flattening of the profile with redshift, which appears to extend to $z > 1.2$. Given that the average profile can be biased toward cool cores (which have very high central density), we also show the median profile in the upper right panel. The median profile is computed by taking the median density at each radius for all clusters within a given redshift range. This panel demonstrates that the median cluster at $1.2 < z < 1.9$ has no visible cusp in the inner density profile ($d\rho_g/dr \sim 0$ for $r < 0.1R_{500}$). These data show that, while some clusters at $z \sim 1.6$ have central density cusps (see also Brodwin et al. 2016), they are in general less peaky than their low-z counterparts.

In the lower panels of Figure 2, we show the electron density profiles in absolute terms, without scaling for the evolving critical density of the universe ($\rho_{\rm crit}$) or to the evolving (and mass-dependent) scale radius (R_{500}). These plots highlight what is physically happening to the cluster and help to clarify the origin of the evolving profiles shown in the upper panels of the figure and in McDonald et al. (2013). In the centers of clusters ($r \sim 10$ kpc) at all redshifts, the median electron density is ~ 0.01 cm^{-3}, with a measured scatter across five redshift bins of only ~10%. From this common point at the center, the high-z cluster profiles have a shallower inner slope and a steeper outer slope than their low-z counterparts. Likewise, the average profiles have a very small scatter (<20%) in central densities over $0 < z < 1.9$. Given that, over the same redshift range, the critical density of the universe changes by a factor of >5, it is unsurprising that the central values of $\rho_g/\rho_{\rm crit}$ show such a strong evolution (upper panels).

3.1.1. Deviations from Self-Similarity

In the previous section, we claim qualitatively that the ICM density profile is self-similar at large radii, consistent with many previous works (e.g., Vikhlinin et al. 2006; Croston et al. 2008; Mantz et al. 2015, 2016). Here, we attempt to quantify this degree of self-similarity for the full sample of clusters shown in Figure 1. We define 20 radial bins (in terms of r/R_{500}; see Section 2.3.1), measuring the gas density in each radial bin for each cluster in our sample. We then fit a function of the

Table 1
X-Ray Properties of SPT-Hiz Sample

Name	R.A. (°)	Decl. (°)	z	M_{500} ($10^{14}\,M_{\odot}$)	R_{500} (Mpc)	Peak		Centroid	
						$a_{\rm phot}$	$n_{e,0}$ ($10^{-2}\,{\rm cm}^{-3}$)	$a_{\rm phot}$	$n_{e,0}$ ($10^{-2}\,{\rm cm}^{-3}$)
SPT-CLJ0156-5541	29.0405	−55.6976	1.281	$3.90^{+0.57}_{-0.40}$	0.69	$0.09^{+0.25}_{-0.06}$	$0.83^{+0.17}_{-0.14}$	$0.09^{+0.10}_{-0.05}$	$0.81^{+0.06}_{-0.06}$
SPT-CLJ0205-5829	31.4459	−58.4849	1.322	$3.44^{+0.63}_{-0.40}$	0.65	$0.73^{+0.36}_{-0.20}$	$0.93^{+0.37}_{-0.27}$	$0.55^{+0.36}_{-0.18}$	$0.60^{+0.24}_{-0.17}$
SPT-CLJ0313-5334	48.4813	−53.5718	1.474	$2.01^{+1.54}_{-0.31}$	0.56	$0.12^{+0.64}_{-0.20}$	$0.75^{+0.41}_{-0.26}$	$0.11^{+0.38}_{-0.21}$	$0.64^{+0.37}_{-0.24}$
SPT-CLJ0459-4947	74.9240	−49.7823	1.85[a]	$2.40^{+0.25}_{-0.27}$	0.49	$0.46^{+0.07}_{-0.09}$	$4.54^{+1.43}_{-1.09}$	$0.51^{+0.07}_{-0.10}$	$1.98^{+0.21}_{-0.19}$
SPT-CLJ0607-4448	91.8940	−44.8050	1.482	$2.65^{+0.55}_{-0.36}$	0.56	$0.07^{+0.05}_{-0.03}$	$5.98^{+1.61}_{-1.27}$	$0.10^{+0.05}_{-0.05}$	$3.81^{+1.58}_{-1.12}$
SPT-CLJ0640-5113	100.0720	−51.2176	1.313	$2.92^{+0.61}_{-0.24}$	0.63	$0.08^{+0.03}_{-0.02}$	$3.03^{+0.61}_{-0.51}$	$0.07^{+0.03}_{-0.02}$	$3.30^{+0.55}_{-0.47}$
SPT-CLJ2040-4451	310.2417	−44.8620	1.478	$3.10^{+0.79}_{-0.47}$	0.60	$0.35^{+0.22}_{-0.12}$	$1.91^{+0.91}_{-0.62}$	$0.36^{+0.26}_{-0.14}$	$0.54^{+0.22}_{-0.16}$
SPT-CLJ2341-5724	355.3533	−57.4166	1.258	$3.37^{+0.70}_{-0.34}$	0.67	$0.28^{+0.05}_{-0.04}$	$2.09^{+0.34}_{-0.29}$	$0.18^{+0.05}_{-0.03}$	$2.70^{+0.60}_{-0.49}$

Notes. Properties of the clusters in the SPT-Hiz sample. Unless otherwise noted, quoted redshifts are based on spectroscopy of ∼5–10 members per cluster. All eight of these clusters have deep *Chandra* observations from which we derive M_{500} based on the $M_{\rm gas}$–M relation from Vikhlinin et al. (2009). We provide a quantitative estimate of the X-ray asymmetry ($a_{\rm phot}$) and the central electron density (n_e) measured with reference to the X-ray peak, as well as the large-scale centroid of the X-ray emission measured in an annulus from 250 to 500 kpc.

[a] Redshift is derived based on a combination of *HST* and *Spitzer* red sequences, along with X-ray spectroscopy (see Section 2.1.1).

form $n_e(r/R_{500}) \propto E(z)^C$ within each radial bin, determining the redshift dependence of the density profile at that radius. If the gas density profile evolves self-similarly, then it should evolve like $\rho_{\rm crit}$, which scales like $E(z)^2$. In Figure 3, we show how C scales with radius. We find that, at $r \gtrsim 0.2R_{500}$, the density profiles are fully consistent (at the 1σ level) with self-similar evolution ($C = 2$). This is consistent with simulations (see, e.g., Kravtsov & Borgani 2012), data from other surveys (see, e.g., Mantz et al. 2016), and the general intuition that gravity is the dominant physics at these radii. The large uncertainty in the measurement of C at $r > R_{500}$ is a result of the background emission dominating by a substantial margin at these radii, leading to relatively large systematic uncertainties in the gas density measurement.

At small radii ($r < 0.2R_{500}$), the measured value of C decreases, from $C = 2$ at $r = 0.2R_{500}$ to $C \sim 0$ at $r \sim 0.01R_{500}$. This implies a breaking of self-similarity in dense cluster cores, where other baryonic physics phenomena (i.e., stellar feedback, AGN feedback, cooling, sloshing, etc.) are important. At the centers of clusters, we find no evidence for redshift dependence on the ICM density ($C = 0.2 \pm 0.5$), which is akin to the unevolving entropy in cluster cores that we reported in McDonald et al. (2013). If this result is interpreted as AGN feedback regulating the inner density profile and balancing the multiphase condensation in an inside-out way (e.g., Gaspari et al. 2014; Voit et al. 2015), then it implies that the impact of AGN feedback is confined to $r \lesssim 0.2R_{500}$.

While it has long been understood that the density cusps of cool core clusters represent a likely deviation from self-similar evolution, we have now directly shown that this is the case using ICM density profiles for clusters spanning $0 < z < 1.9$. We find no evidence that the cores of clusters evolve self-similarly, with self-similar evolution being ruled out at $>3\sigma$ confidence.

3.1.2. Cool Core Evolution

In Figure 4, we examine the evolution of the core ICM density more closely, showing the individually measured central ($r < 0.012R_{500}$) densities for all of the clusters considered in this work. For this figure, we define the cluster center in two ways, as described in Section 2.2: the peak of the X-ray emission and the large-scale centroid. We find no measurable evolution in the mean, maximum, or minimum central densities over the full redshift range explored here, independent of the choice of centering method. We note that the centering choice for the clusters from Vikhlinin et al. (2009) is slightly different than ours, such that it matches the peak selection for relaxed clusters and the centroid selection for disturbed clusters. As such, it is best compared to the maximum peak density and the minimum centroid density. With the exception of the Phoenix cluster at $z = 0.597$ (McDonald et al. 2012), there is a fairly consistent maximum central density of $n_{e,0} \sim 0.08\,{\rm cm}^{-3}$ and a fairly consistent minimum density of $\sim 0.003\,{\rm cm}^{-3}$. Assuming average core temperatures of ∼5 keV, these maxima and minima correspond to central cooling times of 0.5 and 11.2 Gyr, respectively. The lack of evolution in the distribution of central densities (and, by extension, cooling times) suggests that the fraction of cool cores—and the properties of these cores—is relatively stable over the redshift range covered (see also Vikhlinin et al. 2007; Santos et al. 2008, 2010; McDonald et al. 2013). If there were a higher or lower fraction of cool/noncool cores at high-z than at low-z, we would expect this to manifest in the measured averages.

We note that, while we attempt to mask the point sources, there may be contributions to the surface brightness (and gas density) profile from undetected point sources. Assuming a realistic source density, these will have a negligible effect at large radii but could bias the density high in the innermost bins. This is an issue that we cannot address with the available data, but we note that all of the trends reported here are the same whether we consider the central density or the second radial bin, suggesting that X-ray-bright central AGNs are not driving our results.

We next consider the shape of the cool cores as a function of redshift. To determine the radial cool core profile, we subtract the average noncool core profile from each cool core cluster and stack the residuals. This procedure is shown for a

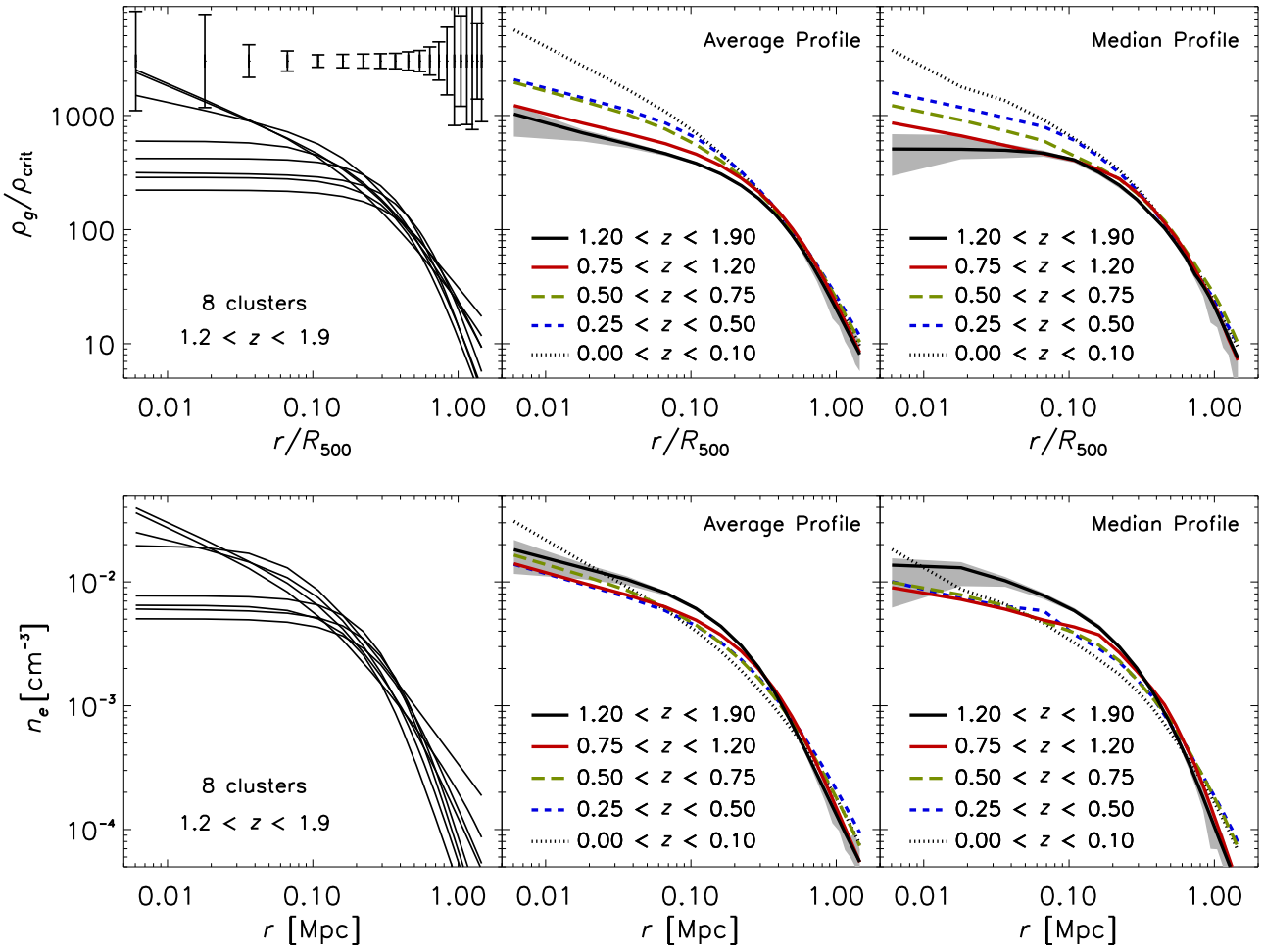

Figure 2. Upper left: normalized gas density (ρ_g/ρ_{crit}) vs. normalized radius (r/R_{500}) for the eight clusters in the SPT-Hiz sample. This panel highlights the large scatter in the cores, where nongravitational processes such as cooling and feedback can shape the density profile, compared to the small scatter at large radii ($>0.2R_{500}$), where clusters are remarkably self-similar. Typical measurement uncertainties in each radial bin are shown at the top and are dominated by small-number statistics at small radii and uncertainty in the background at large radii. Upper middle: average profiles in five different redshift bins. This panel demonstrates that ρ_g/ρ_{crit} in the centers of clusters has increased steadily by a factor of $\sim$5 over the past $\sim$10 Gyr. Outside of the core ($r > 0.1R_{500}$), the density profiles appear to be remarkably self-similar. For clarity, the gray shaded area shows the 1σ uncertainty in the mean profile for the high-z systems only. Upper right: similar to the upper middle panel but for the median profile, which is less sensitive to single extreme systems. The lack of a measurable cusp in the high-z median implies that the first cool cores may have formed around $z \sim 1.6$. For clarity, the gray shaded area shows the 1σ uncertainty in the mean profile for the high-z systems only. Lower panels: similar to the upper panels but for absolute rather than normalized ICM density vs. physical radius. These panels demonstrate that much of the "evolution" observed in the upper panels may be due to an unevolving central density coupled with an evolving value of ρ_{crit}. The scatter in median central ($r < 0.012R_{500}$) density over the five redshift bins shown here is only $\sim$10%.

single cluster in the inset of Figure 5. Here, we define noncool and cool cores as having $n_{e,0} < 0.5 \times 10^{-2}$ and $n_{e,0} > 1.5 \times 10^{-2}\,\mathrm{cm}^{-3}$, respectively, avoiding the "moderate cool core" regime (see, e.g., Hudson et al. 2010). Each of these divisions (cool core, moderate cool core, and noncool core) contains roughly one-third of the cluster sample. The average cool core profile, derived from 49 cool core clusters spanning $0 < z < 1.9$, is shown as the gray shaded region in Figure 5 and is well fit by a β-model with a core radius of $\sim$20–30 kpc. Integrating this profile yields a total cool core gas mass of $\sim 3.5 \times 10^{12}\,M_\odot$, compared to a median total gas mass for these clusters of $5.5 \times 10^{13}\,M_\odot$.

When we divide the cool core sample into redshift slices, we find no evolution in the shape of the cool core. Within the uncertainties, the four residual profiles, spanning $z = 0$ to $z = 1.2$, lie on top of each other. The only exception to this is the highest-redshift bin, where the core appears to be considerably smaller in radius. We caution that this result is at the $\sim 2\sigma$ level and is based on only four cool core clusters identified at $z > 1.2$. It is nonetheless intriguing and may be an indication that we are approaching the epoch of cool core formation at $z \sim 1.6$.

The combination of Figures 4 and 5 demonstrates that the fraction of clusters harboring cool cores and the central density and size/shape of the cool cores have not evolved significantly in the past $\sim$9 Gyr ($z \lesssim 1.2$). The fact that cool cores are confined to the inner $\sim$100 kpc at all redshifts is consistent with the idea that, on large scales, cool and noncool cores are indistinguishable (e.g., Medezinski et al. 2017). The data hint at an epoch of core formation at $z > 1.2$, but with only eight clusters at such high redshifts, this result is not statistically significant.

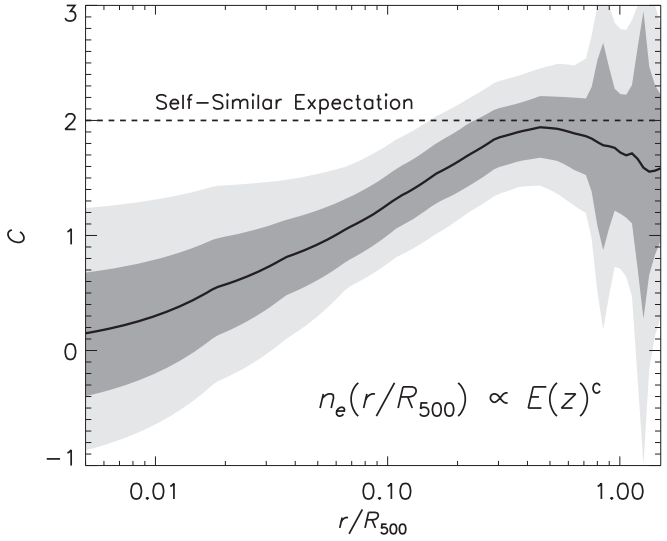

Figure 3. Degree to which the radial ICM density profile evolves as a function of redshift. We assume an evolution of $n_e(r/R_{500}) \propto E(z)^C$, with values of $C = 0$ and $C = 2$ representing no evolution and self-similar evolution, respectively. Shaded dark and light regions correspond to 1σ and 2σ confidence intervals, respectively. This figure demonstrates that, at the centers of clusters, there is no dependence of the gas density on the cluster redshift, while at $r \gtrsim 0.2R_{500}$, the evolution is fully consistent with the self-similar expectation. This result supports a picture in which the evolution of the core is dictated by local processes (e.g., AGN feedback, stellar feedback, cooling), while the large-scale gas distribution is dictated by gravity.

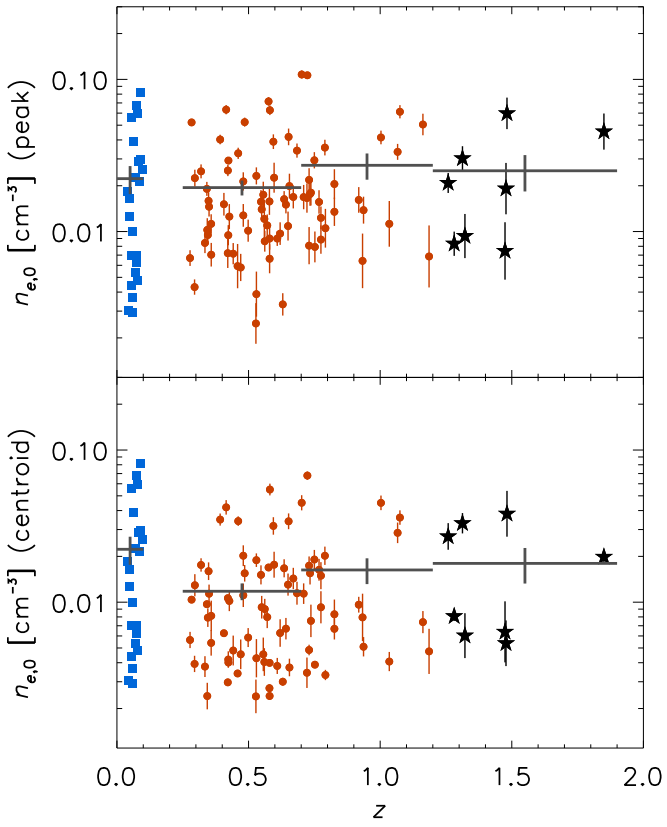

Figure 4. Central deprojected ICM density, as measured in the bin $0 < r < 0.012R_{500}$, centered on the peak (upper panel) and centroid (lower panel) of the X-ray emission. Point types and colors are as defined in Figure 1 and correspond to the three different cluster samples used in this work. The large black crosses show the mean and error on the mean for four different redshift bins, demonstrating no measurable evolution in the typical central density of the ICM over ∼9.5 Gyr.

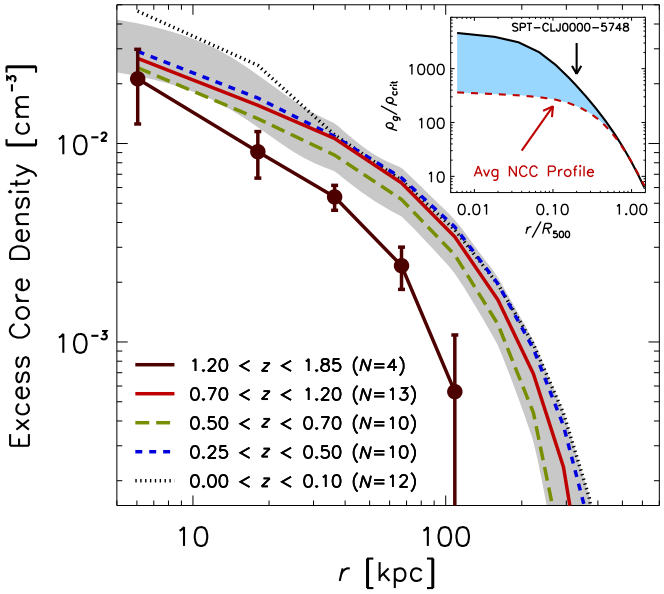

Figure 5. Mean overdensity profile for cool cores as a function of redshift. For each cool core cluster ($n_{e,0} > 1.5 \times 10^{-2}$ cm^{-3}), we subtract the average noncool core profile (based on 33 clusters), as shown in the inset in the upper right. The blue shaded region represents the residual overdensity as a function of radius for this one cluster. In each redshift bin, we average these overdensity profiles, yielding the curves shown in the larger panel. The gray shaded region represents the mean and 1σ scatter for the full sample of cool cores. This figure demonstrates that the normalization and size of cool cores has not evolved in a significant way since $z \sim 1.2$, with a hint ($\sim 2\sigma$, based on only four clusters) of evolution in the highest redshift bin.

3.2. X-Ray Morphology

The X-ray morphology of a galaxy cluster is commonly used as a probe of the cluster's dynamical state (e.g., Mohr et al. 1995; Schuecker et al. 2001; Weißmann et al. 2013; Mantz et al. 2015). Nurgaliev et al. (2017) demonstrated that the measured value of $a_{\rm phot}$, which we use in this work to quantify morphology, is significantly elevated during a major merger for ∼1–2 Gyr, based on hydrodynamic simulations of 26 major ($M_1/M_2 > 0.5$) cluster mergers. This implies that the redshift evolution of $a_{\rm phot}$ ought to roughly probe the evolution of the merger rate over the redshift range considered here. Before providing quantitative results, however, we consider the X-ray images themselves in an attempt to draw qualitative conclusions on the morphological evolution of massive clusters.

In Figure 6, we show Gaussian and adaptively smoothed (using CSMOOTH[16]) 0.5–4.0 keV images of the eight clusters in our high-z sample. The adaptive smoothing parameters were chosen to highlight substructure while avoiding the identification of noise peaks as significant. The latter condition was tested on dozens of images of the Bullet and El Gordo clusters, subsampled to 2000 counts each, in order to determine the appropriate CSMOOTH parameter settings to maximize resolution while minimizing false detections of substructure. This figure demonstrates that the X-ray morphologies of these high-z clusters are not dramatically different from their low-z counterparts. We see evidence for highly disturbed (elongated) systems (e.g., SPT-CLJ2040-4451 and SPT-CLJ2341-5724), systems with cores offset from their centroid that are likely sloshing (e.g., SPT-CLJ0459-4947 and SPT-CLJ0205-5829), and relatively

[16] http://cxc.harvard.edu/ciao/ahelp/csmooth.html

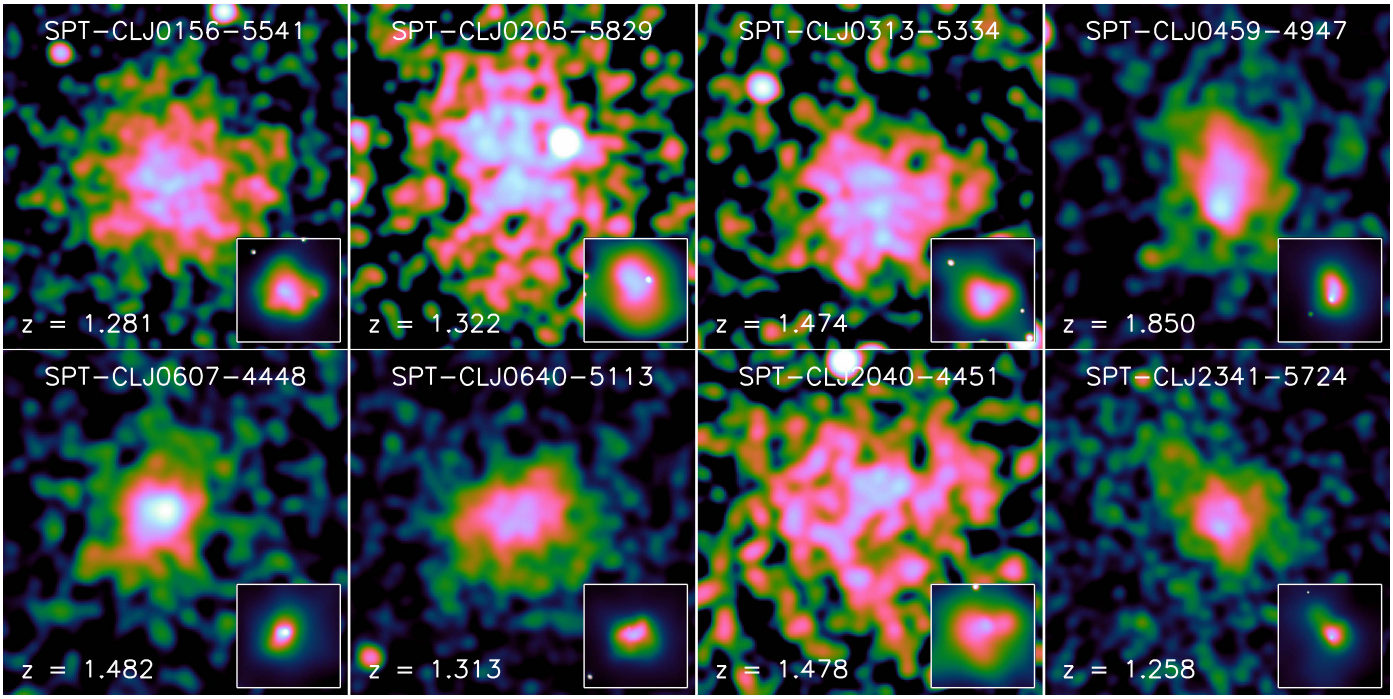

Figure 6. The 0.5–4.0 keV X-ray images of the eight clusters in the SPT-Hiz sample. Each image spans $3 \times R_{500}$ on a side and has been smoothed with a fixed-width Gaussian with FWHM $= 5''$. In the insets, we show adaptively smoothed images, where the smoothing conditions have been chosen to suppress noise and highlight real structure. As discussed in Section 3.1, this smoothing has been tested on low-z, high signal-to-noise data to ensure that noise peaks are not being identified as real structures. This figure shows the diversity of X-ray morphologies for the eight clusters in our sample.

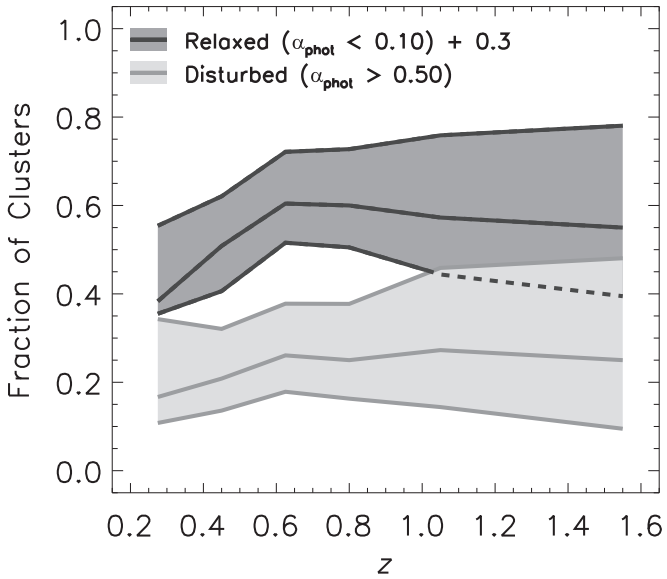

Figure 7. Disturbed (light gray) and relaxed (dark gray) fractions as a function of redshift for the SPT-XVP and SPT-Hiz samples, as derived from the X-ray morphology. These fractions are calculated in six independent redshift bins ($z = 0.2$–0.35, 0.35–0.55, 0.55–0.7, 0.7–0.9, 0.9–1.2, and 1.2–1.9). The relaxed fraction has been offset by $+0.3$, to allow a more straightforward visual comparison. We have chosen to show only the extremes of the morphological distribution here, excluding all clusters near the relaxed/disturbed boundary. The choice of threshold $a_{\rm phot}$ values for classification as disturbed or relaxed is arbitrary and does not drive the result. We find that there is no strong evolution in the fraction of clusters with symmetric or highly asymmetric X-ray morphologies.

relaxed systems (e.g., SPT-CLJ0607-4448 and SPT-CLJ0640-5113). We find no obvious major mergers (i.e., two distinct, highly separated peaks). With the limited signal-to-noise of these exposures, there is no obvious qualitative bias in the morphology of these clusters when compared to the lower-z systems in the full SPT-XVP sample (Nurgaliev et al. 2017).

We consider the dependence of the morphologically disturbed and relaxed fractions as a function of redshift in Figure 7. In this figure, we arbitrarily define "relaxed" as having $a_{\rm phot} < 0.1$ and "disturbed" as having $a_{\rm phot} > 0.5$. The latter is somewhat motivated by simulations (Nurgaliev et al. 2017) and is approximately representative of major (nearly equal-mass) mergers. We note that the choice of threshold does not drive our result. The results of Figure 7 are somewhat surprising: we see no significant evolution in the disturbed or relaxed fraction over the full redshift range studied here. This is consistent with what was found by Nurgaliev et al. (2017) for an SPT-selected sample spanning a smaller redshift range and is seemingly at odds with the increasing merger rate with redshift predicted by simulations (e.g., Fakhouri et al. 2010). The implication of this result is that, over the past $\sim$10 Gyr, there has been no measurable increase in the frequency of major mergers in the most massive clusters. This would either imply that these halos assemble rapidly at $z \gtrsim 2$, followed by a slow growth fueled primarily by minor mergers, or that we are missing an important piece of the puzzle.

Overall, we find no obvious difference in X-ray morphology between our low-z ($0.25 < z < 1.2$) and high-z ($1.2 < z < 1.9$) cluster samples. We will discuss possible reasons for this lack of evolution in Section 4.1. We note that, given the relatively low signal-to-noise ratio of these data compared to well-studied low-redshift clusters, we cannot make any claims on the evolution of more subtle substructure, such as core sloshing, cold fronts, or shocks. Such features require significantly deeper observations to identify.

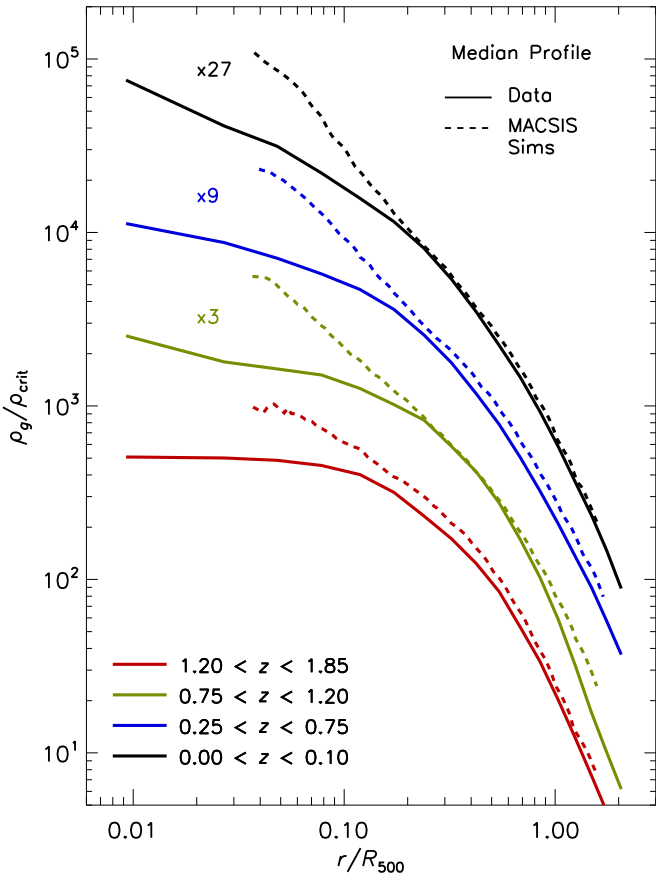

Figure 8. Median gas density profiles for observed clusters in four different redshift ranges (solid lines). Profiles have been scaled by arbitrary factors (1, 3, 9, and 27) to improve clarity. We also show (dotted lines) clusters from the MACSIS simulations (Barnes et al. 2017) that have been matched in redshift and mass to the observed systems. At large radii, there is excellent agreement between the data and simulations. At small radii ($\lesssim 0.1R_{500}$), the simulated clusters are factors of ∼2–3 times more dense than their observed counterparts. This disagreement is most likely due to complex interactions between the radio jets in the central AGN and the cooling ICM that are not being fully captured by the simulations.

4. Discussion

4.1. ICM Density Profiles: Comparison to Simulations

In McDonald et al. (2014), we compared the average pressure profiles of clusters from $z \sim 0$ to $z \sim 1$ to the latest simulations at the time. Here, we compare the measured density profiles over a larger redshift range to the more recent MAssive ClusterS and Intercluster Structures (MACSIS) simulations (Barnes et al. 2017). These simulations track 390 clusters over a large range in cosmic time and mass, including approximations of various baryonic physics processes. Clusters are identified in a large-volume (3.2 Gpc) dark-matter-only simulation with a mass resolution of $5.43 \times 10^{10}\,M_\odot/h$ and softening length of 40 kpc and then resimulated with hydrodynamics at an improved resolution with a mass resolution of $4.4 \times 10^9\,M_\odot/h$ and softening length of 3 kpc. For details of these simulations, see Barnes et al. (2017). From this sample of simulated clusters, we select subsamples at mean redshifts of $\langle z \rangle = 0.0, 0.5, 1.0, 1.5$ and with median masses matching those of the observed clusters at each redshift. In Figure 8, we show the median gas density profiles, normalized to the critical density, in these four redshift bins for both the observed and simulated clusters. In general, the simulated and observed clusters appear similar at $r > 0.2R_{500}$, suggesting that the large-scale physics is being properly captured in these simulations. We find offsets of ∼10% in normalization between the real and simulated clusters, which may be due to a number of small differences, including the mean mass per particle (in converting from electron density to mass density), the distribution of masses (low-mass clusters will scatter low in ρ_g/ρ_{crit}; Vikhlinin et al. 2006), the cluster gas fractions, or the cosmology assumed. These offsets are small and signify that the physics of the ICM is well described by simulations outside of cluster cores. In the cores ($r < 0.1R_{500}$), simulated clusters have a factor of ∼2–3 higher density than observed clusters at the same redshift, suggesting that the included physics may be insufficient to describe the complex interplay between the central radio-loud AGN, its host giant elliptical galaxy, and the dense cluster core. This is similar to what was reported in McDonald et al. (2014) when comparing to simulations from Battaglia et al. (2012) and Bocquet et al. (2016) and is a long-standing problem with creating realistic clusters in cosmological simulations (for a review, see Kravtsov & Borgani 2012). This issue appears to be present at all epochs, with clusters at $1.2 < z < 1.9$ having overdense cores in simulations compared to observations at the same redshift. Within the uncertainty, we measure no significant improvement in the data–simulation comparison in cluster cores over the full redshift range probed here.

In summary, we find that the latest MACSIS simulations (Barnes et al. 2017) yield a good match to the observed density profiles of clusters in this work at $r > 0.2R_{500}$. In cluster cores, the simulations overpredict the ICM density by a factor of ∼2–3 at all redshifts.

4.2. Understanding the Evolution of Cluster Cores

In Section 3.1, we showed that the inner slope of the median gas density profile has evolved significantly over the past ∼10 Gyr. We investigate whether this is due to mass evolution in our sample by first isolating a narrow range in mass and considering the redshift dependence and then isolating a narrow range in redshift and considering the mass dependence. For this test, we include lower-mass systems from Vikhlinin et al. (2009) for a direct (nonevolving) comparison to the low-mass systems at $z > 1.2$. In Figure 9, we show the results of this test, where we have used coarser redshift bins than in Figure 2, since the number of clusters in the narrow mass range is small. We find that, even in a very narrow mass range ($14.3 < \log_{10} M_{500} < 14.6$), there is a strong redshift dependence, with the low-z clusters having significantly cuspier density profiles than their high-z counterparts. In contrast, if we consider an order of magnitude range in mass at roughly fixed redshift ($0.25 < z < 0.55$), we measure no significant variation in the median gas density profile. This suggests that the core evolution shown in Figure 2 and reported in McDonald et al. (2013) is not a byproduct of the mass evolution of clusters but is indeed a steady change in the median density slope over the past ∼10 Gyr for clusters at a fixed mass.

Figures 2–5 reveal several important features about the ICM density profiles in massive clusters. Namely, we find remarkable similarity in the absolute properties of cool cores as a function of redshift, including the distribution of core densities, the average

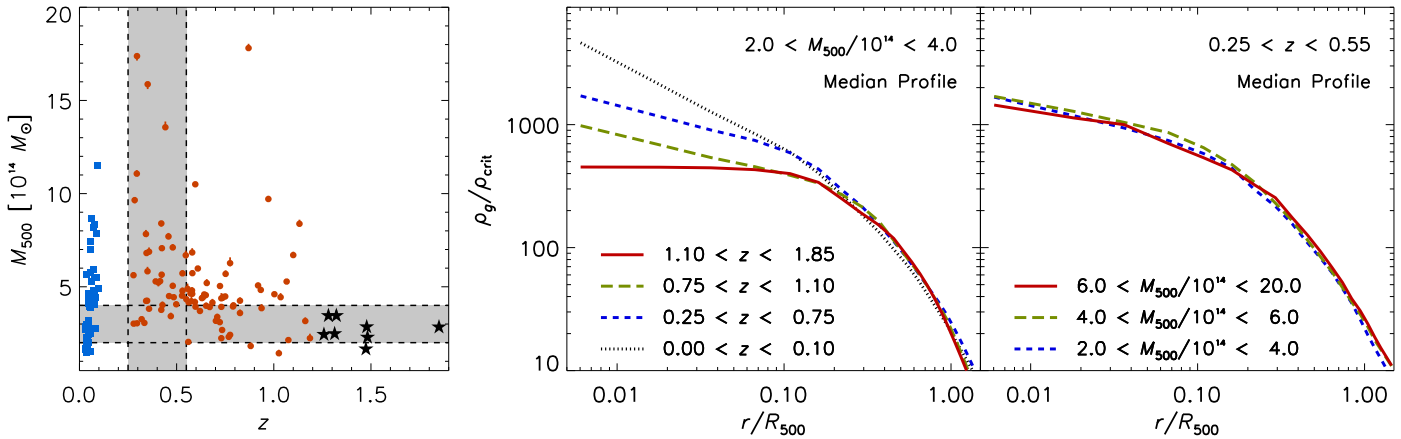

Figure 9. Left panel: distribution of galaxy cluster masses and redshifts used in this work. For the low-z subsample here, drawn from Vikhlinin et al. (2009), we consider a broader mass range than in the previous plots. Gray shaded regions represent cuts for two subsamples: a large mass range at nearly fixed redshift and a large redshift range at nearly fixed mass. Center panel: median density profiles for clusters over a broad redshift range and narrow mass range. This shows the same evolution as in Figure 2, suggesting that this was not a result of a mass bias between redshift bins. Right panel: median density profiles for clusters over a broad mass range and narrow redshift range. These median profiles are indistinguishable, suggesting that there is no mass dependence driving our results in Figure 2.

central density, and the shape of the cool core excess density profile. The lack of observable evolution in any of these properties suggests that the three-dimensional shape and quasi-thermal equilibrium of cool cores were established early in the evolution of clusters. These properties have been maintained over timescales significantly longer than the cool core cooling time, suggesting that the source of feedback that is offsetting cooling is tightly self-regulated. Such a tight loop between the cool core properties and the feedback response can be achieved via chaotic cold accretion, i.e., cold clouds and filaments condensing out of the hot ICM and being efficiently funneled toward the black hole via inelastic collisions (e.g., Gaspari et al. 2017; Prasad et al. 2016; Tremblay et al. 2016), triggering the immediate AGN outflow response and thus preventing the catastrophic steepening of the density profiles.

At the same time, we find no evidence for departures from self-similar evolution at radii larger than $0.2R_{500}$. Interestingly, this is precisely the radius at which the average temperature profile for cool core clusters deviates from that of noncool core clusters (Vikhlinin et al. 2006; Baldi et al. 2012). We conclude that, to within the precision of our measurements, the ICM density profile has evolved self-similarly at $r > 0.2R_{500}$ over the past $\sim$10 Gyr.

The above two paragraphs describe a scenario in which the properties of cool cores are locked in early while the rest of the cluster evolves in a predictable fashion that is well described by simple models of gravitational collapse (see, e.g., Kravtsov & Borgani 2012). This two-stage evolution is demonstrated in Figure 10. This figure shows that the evolution in cuspiness that we see in Figure 2 and that was previously reported by Vikhlinin et al. (2007), Santos et al. (2008, 2010), and McDonald et al. (2013) can be reproduced with a nonevolving core embedded in a self-similarly evolving cluster. The evolving cuspiness in this scenario is due to the increasing contrast between the dense cool core and the rest of the cluster, which, at high-z, is at higher density for a given r/R_{500}.

At first, this result appears to contradict the evolving core mass presented in McDonald et al. (2013). In that work, the mass of the cool core was defined as the difference between the cool core and average noncool core profile (as defined here) but only integrated to $0.1R_{500}$. Because R_{500} is a physically smaller radius for high-z clusters, this meant that we were integrating over much less of the core volume for high-z clusters than for their low-z counterparts. Since the cool core does not appear to be evolving in size, it makes more sense to define the outer radius in physical units (i.e., 100 kpc) rather than relative units (i.e., $0.1R_{500}$).

In summary, we find that the evolution in the ICM density profiles for massive clusters from $z = 0$ to $z \sim 1.6$ is well described by the sum of a self-similarly evolving noncool core profile and a nonevolving cool core. This simple picture describes the results presented here (Figures 2–5) and in previous works (e.g., Vikhlinin et al. 2007; Santos et al. 2008, 2010; McDonald et al. 2013). The size of the unevolving core, approximately 100–200 kpc, provides a rough boundary within which the similarity-breaking feedback mechanism (i.e., AGN feedback) must do work. The fact that the core has remained stable in size and mass over such a long time period indicates that AGN feedback must be tightly regulated and gentle, rather than being injected via a strong quasar blast (Gaspari et al. 2014).

4.3. The Evolution of the Halo Merger Rate

In Figure 7, we show that the fraction of clusters identified as disturbed based on asymmetry in the X-ray emission has not changed significantly from $z \sim 0.2$ to $z \sim 1.4$. This appears to contradict the prediction from simulations that the merger rate is a strong function of redshift (see, e.g., Fakhouri & Ma 2010) but is consistent with other groups that have studied the evolution of cluster morphology (e.g., Mantz et al. 2015; Nurgaliev et al. 2017). For the most massive halos ($M > 10^{14}\,M_\odot$), Fakhouri & Ma (2010) found that the rate of major ($M_1/M_2 > 0.3$) mergers, dN_m/dt, increases from $\sim$0.07 Gyr^{-1} at $z \sim 0$ to 0.2 Gyr^{-1} at $z \sim 1$, or roughly a factor of 3 increase over the past $\sim$8 Gyr. However, to go from a predicted halo merger rate to an observed disturbed fraction, we must assume a timescale over which the X-ray emission would appear disturbed after a major merger (the "relaxation time"). The simplest choice of relaxation time would be one that is constant with redshift, meaning that the observed disturbed fraction would trace the halo merger rate. Figure 11 shows how poorly this choice of timescale fares when compared

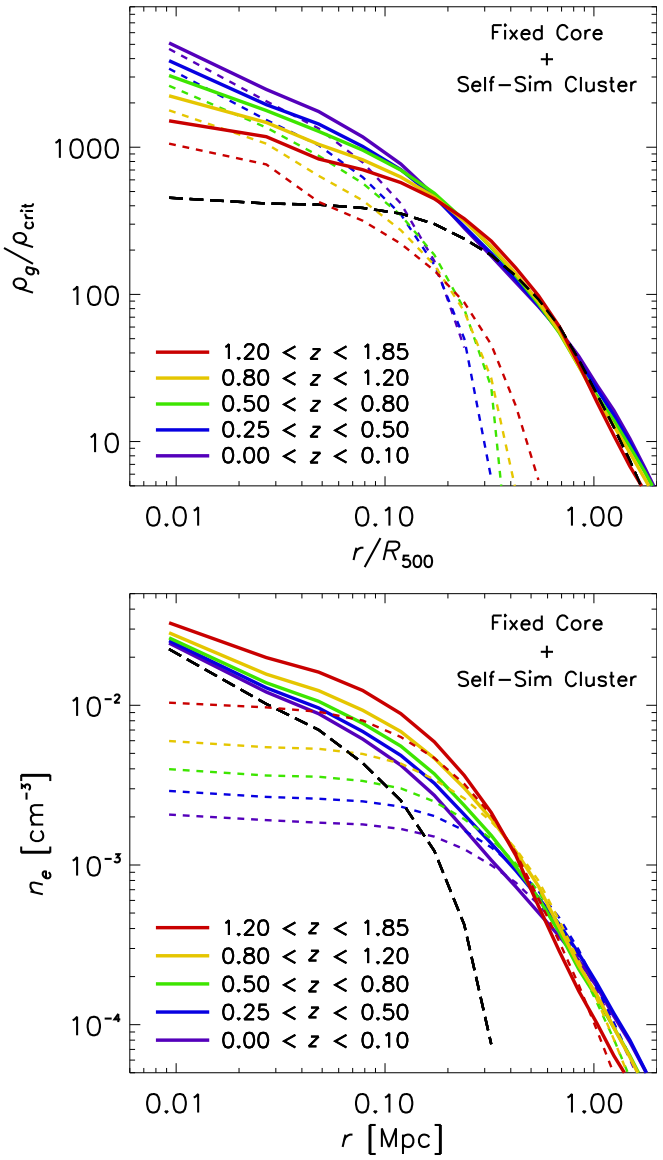

Figure 10. Upper panel: expected density profiles (solid lines) for a self-similarly evolving, noncool core cluster (dashed black line) combined with a nonevolving cool core (dotted colored lines). Because of the choice of scaling, the nonevolving cool core term appears to be evolving. Lower panel: same as top panel but for the profiles in absolute physical units. Without any cosmological scaling, the cool core now appears nearly static, while the bulk of the cluster shows the expected self-similar evolution.

to the data from both this work and Mantz et al. (2015).[17] At the highest redshifts probed, the predicted evolution is inconsistent with the observations at the >97% confidence level, suggesting that the choice of a constant relaxation time is a poor one.

However, if we modify our assumption about how long a cluster will appear disturbed in the X-ray after a major merger, we predict a dramatically different evolution. Assuming self-similar growth of clusters, the crossing time ($\tau_{cr} \propto R/\sigma \propto H(z)^{-1}$; Carlberg et al. 1997) ought to be shorter at early times. Under the assumption that a cluster appears disturbed for approximately a crossing time (or

[17] We use the "symmetry" (S) parameter from Mantz et al. (2015) to identify disturbed clusters. Using overlapping clusters from the analyses of Mantz et al. (2015) and Nurgaliev et al. (2017), we find that $S < 0.6$ is roughly equivalent to $a_{phot} > 0.5$.

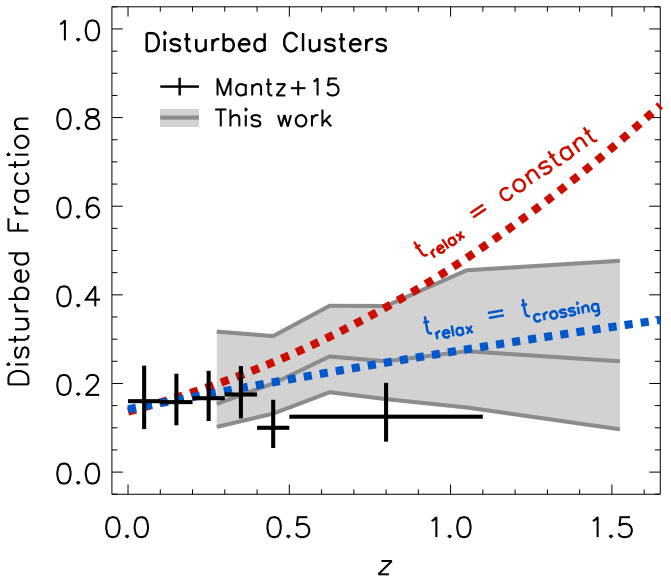

Figure 11. Fraction of observed clusters morphologically classified as disturbed as a function of redshift from Figure 7. We also include data from Mantz et al. (2015), where the disturbed fraction is defined based on their "symmetry" parameter, which we find agrees well with a_{phot} for identifying disturbed systems. We have excluded SPT-selected clusters from the Mantz et al. (2015) study for this comparison. We compare these data to the halo merger rate for massive halos from Fakhouri & Ma (2010), assuming that a cluster appears disturbed after a major merger for a fixed amount of time (red line) or for a crossing time (blue line) and normalizing the profiles to agree with the data at $z \sim 0.1$. The latter agrees well with the data and implies that clusters at early times relaxed faster after a merger than those today due to their lower mass and higher density.

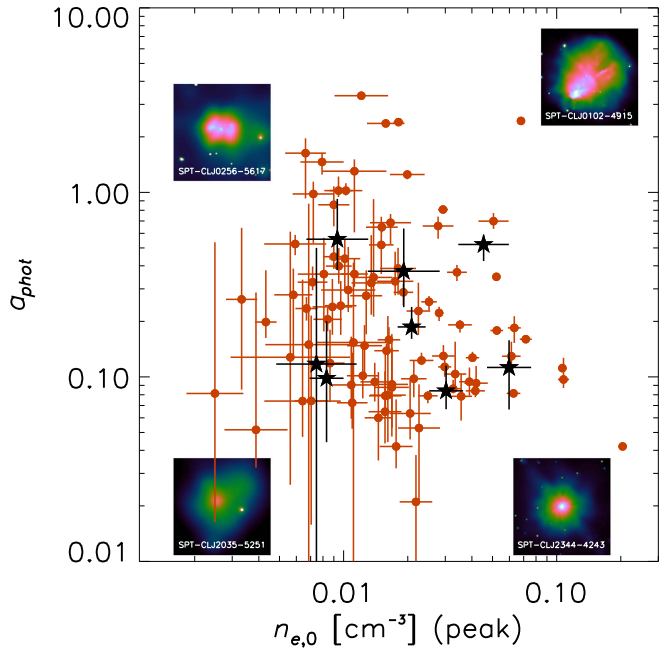

Figure 12. Photon asymmetry (a_{phot}) vs. peak density ($n_{e,0}$) for the clusters in the SPT-XVP (red circles) and SPT-Hiz (black stars) samples. We show small X-ray surface brightness maps for four low-z clusters in the extreme corners of this plot, demonstrating disturbed and relaxed clusters with and without density peaks. The eight high-z clusters span the full range of morphologies, occupying all parts of this parameter space.

that relaxation time is proportional to crossing time), the expected disturbed fraction from simulations is highly suppressed. This is due to the fact that the merger rate is ∼3

times higher at $z \sim 1$ compared to that at $z \sim 0$ (Fakhouri & Ma 2010), while the relaxation time is ~2 times shorter ($H(z)$ is twice as large) over the same redshift interval. Combined, this results in a relatively mild evolution, fully consistent with what is observed (Figure 11).

4.4. Demographics of Massive, High-z Clusters

Using the combination of the peak density and the morphological asymmetry, we can consider cluster morphologies in two dimensions: radial and azimuthal. In Figure 12, we show the distribution of clusters in the SPT-XVP and SPT-Hiz samples in this two-dimensional space, which roughly separates the clusters into four categories: relaxed cool cores, disturbed cool cores, relaxed noncool cores, and disturbed noncool cores. We find that the high-z clusters occupy the full range of parameter space, with each of the four types represented clearly in this sample of eight clusters. Interestingly, one of the 10 strongest cool cores in the full sample is at $z \sim 1.5$, suggesting that cool cores were able to form very early on. Overall, we see no evidence that a specific morphological class is over- or underrepresented in this $z > 1.2$ sample.

5. Summary

We have presented results from an X-ray study of eight SZ-selected galaxy clusters at $z > 1.2$ and $M_{500} > 2 \times 10^{14}\, M_{\odot}$ that were observed recently with the *Chandra X-ray Observatory*. We combine this sample of high-z clusters with samples of 49 massive X-ray-selected clusters at $0 < z < 0.1$ and 90 SZ-selected clusters spanning $0.25 < z < 1.2$, all with existing *Chandra* data, allowing us to track the evolution of the ICM over ~10 Gyr. In this work, we focus specifically on quantities derived based on the X-ray surface brightness and defer a spectroscopic analysis to a future paper. Below, we summarize the main results of this study.

1. We find that, at $r > 0.2R_{500}$, the ICM density profiles of massive galaxy clusters are fully consistent with expectations from self-similar evolution (i.e., $n_e \propto E(z)^2$) over the full redshift range probed here. At $r < 0.2R_{500}$, we find departures from self-similarity, with the centers of clusters showing no significant evolution in gas density ($n_{e,0.01R_{500}} \propto E(z)^{0.2\pm0.5}$).
2. Consistent with earlier works, we find that the central cuspiness of ICM density profiles continues to decrease with increasing redshift, while the absolute central density remains constant, on average.
3. We find that the mean overdensity profile of cool cores does not evolve, with the central density, radial extent, and total integrated mass remaining constant from $z = 0$ to $z = 1.2$. There is an $\sim 2\sigma$ hint of evolution at $z > 1.2$ based on only four cool core clusters at these high redshifts.
4. We propose an evolutionary scenario in which cool cores formed early ($z \gtrsim 1.5$) and their properties (size, mass, and density) have remained fixed, while the bulk of the cluster has grown in size and mass around them. The combination of a fixed core and a self-similarly evolving cluster provides a successful description of our observations and suggests that AGN feedback, mainly affecting the inner ~100 kpc scale, is preserving the core properties for over ~10 Gyr in a gentle and tightly self-regulated way.
5. We find that clusters at $z > 1.2$ span the same range in morphology as those at $z < 0.5$, with no measurable bias toward an overabundance of relaxed or merging systems. This sample of eight systems includes one that we would classify as a relaxed, strong cool core and two that we would classify as being highly disturbed.
6. We confirm and extend previous works by Nurgaliev et al. (2017) and Mantz et al. (2015), who showed that there is no measurable evolution in the fraction of clusters morphologically classified as disturbed (i.e., major mergers). We show that this is consistent with the rapidly rising merger rate predicted by cosmological simulations, if we assume that the relaxation timescales like the crossing time (which, on average, decreases with increasing redshift).

In summary, we find that the properties of the most distant clusters observed with *Chandra* are remarkably similar to those of the well-studied systems at $z \sim 0$. The cores of the clusters appear to be frozen in time, the bulk of the cluster is evolving self-similarly, and the fraction of relaxed/disturbed clusters has not changed significantly. Given the fact that high-redshift clusters are both faint and redshifted to low energy, where current X-ray telescopes are less sensitive, it will be challenging to significantly improve upon the constraints provided here. The combination of future cluster surveys—including those in the SZ, such as SPT-3G (Benson et al. 2014) and Advanced ACT-Pol (Niemack et al. 2010), and the infrared (e.g., WFIRST and Euclid)—and next-generation X-ray telescopes (e.g., Star-X, Athena, and Lynx) will provide orders of magnitude improvement on analyses such as this one and allow us to trace the properties of the ICM back to its appearance at $z \sim 2$–3.

Much of this work was enabled by generous GTO contributions from Stephen S. Murray, the *Chandra* High Resolution Camera PI. The work was in progress at the time of his untimely death in 2015. He was a valued member of the Center for Astrophysics and a strong supporter of SPT science; he will be greatly missed by all of us. Support for this work was provided by the National Aeronautics and Space Administration (NASA) through *Chandra* award number GO5-16141X issued by the *Chandra X-ray Observatory* Center, which is operated by the Smithsonian Astrophysical Observatory (SAO) for and on behalf of NASA under contract NAS8-03060. The South Pole Telescope is supported by the National Science Foundation (NSF) through grant PLR-1248097. Partial support is also provided by the NSF Physics Frontier Center grant PHY-1125897 to the Kavli Institute of Cosmological Physics at the University of Chicago, the Kavli Foundation, and the Gordon and Betty Moore Foundation grant GBMF 947. BB is supported by the Fermi Research Alliance, LLC, under contract no. De-AC02-07CH11359 with the United States Department of Energy. Work at Argonne National Laboratory was supported under U.S. Department of Energy contract DE-AC02-06CH11357. MG is supported by NASA through Einstein Postdoctoral Fellowship award number PF-160137 issued by the *Chandra X-ray Observatory* Center, which is operated by the SAO for and on behalf of NASA under contract NAS8-03060.

Appendix

Below, we list the mean (Table 2) and median (Table 3) density profiles in both normalized and absolute units. These

Table 2
Mean ICM Density Profiles

			z						z		
	0.0–0.1	0.25–0.5	0.5–0.75	0.75–1.2	1.2–1.9		0.0–0.1	0.25–0.5	0.5–0.75	0.75–1.2	1.2–1.9
r/R_{500}			$\log_{10}(\rho_g/\rho_{\rm crit})$			r [kpc]			$\log_{10}(n_e\ [{\rm cm}^{-3}])$		
0.01	3.47 ± 0.11	3.16 ± 0.07	3.09 ± 0.07	2.94 ± 0.09	2.83 ± 0.15	6	−1.82 ± 0.12	−2.02 ± 0.07	−1.99 ± 0.07	−2.00 ± 0.09	−1.87 ± 0.13
0.02	3.26 ± 0.09	3.06 ± 0.05	2.98 ± 0.06	2.84 ± 0.07	2.75 ± 0.11	18	−2.04 ± 0.10	−2.12 ± 0.06	−2.10 ± 0.06	−2.10 ± 0.07	−1.96 ± 0.10
0.04	3.11 ± 0.07	2.98 ± 0.05	2.89 ± 0.05	2.78 ± 0.06	2.69 ± 0.09	36	−2.19 ± 0.08	−2.20 ± 0.05	−2.18 ± 0.05	−2.16 ± 0.06	−2.02 ± 0.08
0.07	2.95 ± 0.06	2.89 ± 0.04	2.80 ± 0.04	2.71 ± 0.05	2.63 ± 0.07	67	−2.33 ± 0.07	−2.29 ± 0.04	−2.28 ± 0.04	−2.24 ± 0.05	−2.11 ± 0.05
0.11	2.80 ± 0.05	2.77 ± 0.03	2.70 ± 0.03	2.63 ± 0.04	2.56 ± 0.05	109	−2.47 ± 0.06	−2.39 ± 0.03	−2.39 ± 0.03	−2.33 ± 0.04	−2.23 ± 0.04
0.16	2.64 ± 0.04	2.64 ± 0.02	2.58 ± 0.02	2.54 ± 0.03	2.48 ± 0.04	161	−2.61 ± 0.05	−2.51 ± 0.03	−2.51 ± 0.02	−2.45 ± 0.03	−2.36 ± 0.03
0.22	2.48 ± 0.03	2.50 ± 0.02	2.46 ± 0.02	2.44 ± 0.02	2.38 ± 0.03	222	−2.75 ± 0.04	−2.65 ± 0.02	−2.64 ± 0.01	−2.57 ± 0.03	−2.52 ± 0.03
0.29	2.33 ± 0.02	2.35 ± 0.01	2.32 ± 0.01	2.32 ± 0.02	2.27 ± 0.03	292	−2.89 ± 0.03	−2.79 ± 0.02	−2.78 ± 0.01	−2.72 ± 0.03	−2.70 ± 0.03
0.37	2.19 ± 0.01	2.20 ± 0.01	2.18 ± 0.01	2.20 ± 0.02	2.14 ± 0.03	370	−3.02 ± 0.02	−2.93 ± 0.02	−2.93 ± 0.01	−2.87 ± 0.03	−2.89 ± 0.04
0.45	2.05 ± 0.01	2.06 ± 0.01	2.05 ± 0.02	2.07 ± 0.02	2.01 ± 0.03	454	−3.15 ± 0.02	−3.06 ± 0.02	−3.07 ± 0.01	−3.03 ± 0.03	−3.07 ± 0.04
0.54	1.92 ± 0.01	1.93 ± 0.02	1.91 ± 0.02	1.93 ± 0.02	1.88 ± 0.02	544	−3.27 ± 0.02	−3.19 ± 0.02	−3.20 ± 0.01	−3.19 ± 0.03	−3.26 ± 0.05
0.64	1.79 ± 0.01	1.80 ± 0.02	1.79 ± 0.02	1.80 ± 0.02	1.74 ± 0.02	638	−3.38 ± 0.02	−3.31 ± 0.02	−3.34 ± 0.02	−3.35 ± 0.04	−3.44 ± 0.07
0.74	1.67 ± 0.01	1.67 ± 0.02	1.66 ± 0.03	1.66 ± 0.03	1.61 ± 0.03	737	−3.50 ± 0.02	−3.43 ± 0.02	−3.47 ± 0.02	−3.50 ± 0.04	−3.60 ± 0.08
0.84	1.55 ± 0.01	1.56 ± 0.02	1.54 ± 0.03	1.53 ± 0.03	1.48 ± 0.04	838	−3.60 ± 0.02	−3.54 ± 0.03	−3.59 ± 0.02	−3.65 ± 0.05	−3.76 ± 0.09
0.94	1.44 ± 0.01	1.45 ± 0.03	1.43 ± 0.03	1.40 ± 0.03	1.35 ± 0.05	941	−3.70 ± 0.02	−3.65 ± 0.03	−3.70 ± 0.02	−3.79 ± 0.05	−3.90 ± 0.10
1.04	1.34 ± 0.01	1.35 ± 0.03	1.32 ± 0.03	1.28 ± 0.04	1.23 ± 0.06	1045	−3.80 ± 0.02	−3.75 ± 0.03	−3.81 ± 0.03	−3.93 ± 0.05	−4.03 ± 0.12
1.15	1.24 ± 0.02	1.25 ± 0.03	1.22 ± 0.04	1.16 ± 0.04	1.12 ± 0.07	1149	−3.89 ± 0.02	−3.84 ± 0.03	−3.91 ± 0.03	−4.05 ± 0.06	−4.16 ± 0.13
1.25	1.14 ± 0.02	1.17 ± 0.03	1.13 ± 0.04	1.06 ± 0.05	1.02 ± 0.08	1252	−3.98 ± 0.02	−3.92 ± 0.03	−4.01 ± 0.03	−4.16 ± 0.06	−4.27 ± 0.14
1.35	1.05 ± 0.02	1.09 ± 0.04	1.04 ± 0.04	0.96 ± 0.05	0.92 ± 0.08	1353	−4.06 ± 0.02	−4.00 ± 0.04	−4.10 ± 0.03	−4.26 ± 0.07	−4.37 ± 0.15
1.45	0.97 ± 0.02	1.01 ± 0.04	0.97 ± 0.04	0.87 ± 0.06	0.84 ± 0.09	1452	−4.14 ± 0.02	−4.08 ± 0.04	−4.18 ± 0.04	−4.36 ± 0.07	−4.46 ± 0.15

Table 3
Median ICM Density Profiles

	z						z				
	0.0–0.1	0.25–0.5	0.5–0.75	0.75–1.2	1.2–1.9		0.0–0.1	0.25–0.5	0.5–0.75	0.75–1.2	1.2–1.9
r/R_{500}			$\log_{10}(\rho_g/\rho_{\rm crit})$			r [kpc]			$\log_{10}(n_e\ [{\rm cm}^{-3}])$		
0.01	3.57 ± 0.14	3.20 ± 0.08	3.09 ± 0.09	2.94 ± 0.11	2.70 ± 0.19	6	-1.74 ± 0.15	-2.00 ± 0.09	-2.00 ± 0.09	-2.05 ± 0.11	-1.91 ± 0.16
0.02	3.25 ± 0.11	3.07 ± 0.07	2.96 ± 0.07	2.82 ± 0.09	2.70 ± 0.14	18	-2.07 ± 0.12	-2.13 ± 0.07	-2.10 ± 0.08	-2.14 ± 0.08	-1.93 ± 0.12
0.04	3.13 ± 0.09	2.98 ± 0.06	2.87 ± 0.06	2.74 ± 0.07	2.69 ± 0.11	36	-2.18 ± 0.10	-2.20 ± 0.06	-2.19 ± 0.06	-2.22 ± 0.07	-2.01 ± 0.09
0.07	2.96 ± 0.08	2.90 ± 0.05	2.78 ± 0.05	2.66 ± 0.06	2.67 ± 0.09	67	-2.33 ± 0.08	-2.23 ± 0.05	-2.32 ± 0.05	-2.31 ± 0.06	-2.11 ± 0.07
0.11	2.80 ± 0.06	2.78 ± 0.04	2.65 ± 0.04	2.61 ± 0.05	2.61 ± 0.06	109	-2.49 ± 0.07	-2.42 ± 0.04	-2.41 ± 0.04	-2.36 ± 0.05	-2.23 ± 0.04
0.16	2.66 ± 0.04	2.64 ± 0.03	2.54 ± 0.03	2.53 ± 0.04	2.50 ± 0.05	161	-2.63 ± 0.06	-2.54 ± 0.03	-2.51 ± 0.03	-2.43 ± 0.04	-2.37 ± 0.03
0.22	2.52 ± 0.03	2.50 ± 0.02	2.44 ± 0.02	2.45 ± 0.03	2.39 ± 0.04	222	-2.75 ± 0.05	-2.65 ± 0.03	-2.64 ± 0.02	-2.57 ± 0.03	-2.53 ± 0.04
0.29	2.37 ± 0.02	2.35 ± 0.02	2.32 ± 0.02	2.32 ± 0.02	2.26 ± 0.03	292	-2.88 ± 0.04	-2.79 ± 0.03	-2.79 ± 0.01	-2.72 ± 0.03	-2.70 ± 0.04
0.37	2.21 ± 0.01	2.19 ± 0.02	2.19 ± 0.02	2.20 ± 0.02	2.13 ± 0.03	370	-3.01 ± 0.03	-2.92 ± 0.03	-2.93 ± 0.01	-2.86 ± 0.03	-2.88 ± 0.05
0.45	2.06 ± 0.01	2.05 ± 0.02	2.08 ± 0.02	2.06 ± 0.02	2.01 ± 0.03	454	-3.15 ± 0.03	-3.08 ± 0.03	-3.05 ± 0.01	-2.99 ± 0.04	-3.06 ± 0.05
0.54	1.92 ± 0.01	1.92 ± 0.02	1.94 ± 0.02	1.93 ± 0.03	1.88 ± 0.03	544	-3.28 ± 0.02	-3.22 ± 0.03	-3.19 ± 0.02	-3.16 ± 0.04	-3.23 ± 0.07
0.64	1.79 ± 0.01	1.78 ± 0.02	1.81 ± 0.03	1.80 ± 0.03	1.75 ± 0.03	638	-3.41 ± 0.02	-3.32 ± 0.03	-3.32 ± 0.02	-3.33 ± 0.05	-3.41 ± 0.08
0.74	1.67 ± 0.01	1.65 ± 0.02	1.69 ± 0.03	1.65 ± 0.03	1.60 ± 0.04	737	-3.52 ± 0.02	-3.46 ± 0.03	-3.46 ± 0.02	-3.48 ± 0.05	-3.59 ± 0.10
0.84	1.55 ± 0.01	1.53 ± 0.03	1.59 ± 0.04	1.52 ± 0.04	1.50 ± 0.05	838	-3.62 ± 0.02	-3.57 ± 0.03	-3.57 ± 0.03	-3.65 ± 0.06	-3.75 ± 0.11
0.94	1.43 ± 0.02	1.44 ± 0.03	1.49 ± 0.04	1.40 ± 0.04	1.39 ± 0.06	941	-3.72 ± 0.03	-3.68 ± 0.03	-3.68 ± 0.03	-3.81 ± 0.06	-3.90 ± 0.13
1.04	1.32 ± 0.02	1.32 ± 0.04	1.39 ± 0.04	1.29 ± 0.05	1.27 ± 0.07	1045	-3.82 ± 0.03	-3.77 ± 0.04	-3.79 ± 0.03	-3.96 ± 0.07	-4.04 ± 0.15
1.15	1.22 ± 0.02	1.23 ± 0.04	1.29 ± 0.05	1.16 ± 0.05	1.16 ± 0.08	1149	-3.92 ± 0.03	-3.86 ± 0.04	-3.88 ± 0.04	-4.10 ± 0.07	-4.17 ± 0.16
1.25	1.12 ± 0.02	1.15 ± 0.04	1.19 ± 0.05	1.04 ± 0.06	1.05 ± 0.09	1252	-4.01 ± 0.03	-3.95 ± 0.04	-3.98 ± 0.04	-4.22 ± 0.08	-4.29 ± 0.17
1.35	1.04 ± 0.02	1.07 ± 0.05	1.10 ± 0.05	0.94 ± 0.06	0.95 ± 0.11	1353	-4.09 ± 0.03	-4.02 ± 0.05	-4.06 ± 0.04	-4.34 ± 0.08	-4.39 ± 0.18
1.45	0.97 ± 0.02	1.00 ± 0.05	1.01 ± 0.05	0.86 ± 0.07	0.86 ± 0.12	1452	-4.17 ± 0.03	-4.10 ± 0.05	-4.14 ± 0.05	-4.44 ± 0.09	-4.49 ± 0.19

data are plotted in Figure 2. Uncertainties quoted are 1σ uncertainties on the mean/median.

References

Allington-Smith, J., Breare, M., Ellis, R., et al. 1994, PASP, 106, 983
Andersson, K., Benson, B. A., Ade, P. A. R., et al. 2011, ApJ, 738, 48
Baldi, A., Ettori, S., Molendi, S., & Gastaldello, F. 2012, A&A, 545, A41
Barnes, D. J., Kay, S. T., Henson, M. A., et al. 2017, MNRAS, 465, 213
Battaglia, N., Bond, J. R., Pfrommer, C., & Sievers, J. L. 2012, ApJ, 758, 74
Bayliss, M. B., Ashby, M. L. N., Ruel, J., et al. 2014, ApJ, 794, 12
Benson, B. A., Ade, P. A. R., Ahmed, Z., et al. 2014, Proc. SPIE, 9153, 1
Bleem, L. E., Stalder, B., de Haan, T., et al. 2015, ApJS, 216, 27
Bocquet, S., Saro, A., Dolag, K., & Mohr, J. J. 2016, MNRAS, 456, 2361
Bocquet, S., Saro, A., Mohr, J. J., et al. 2015, ApJ, 799, 214
Brodwin, M., McDonald, M., Gonzalez, A. H., et al. 2016, ApJ, 817, 122
Brodwin, M., Stanford, S. A., Gonzalez, A. H., et al. 2013, ApJ, 779, 138
Carlberg, R. G., Yee, H. K. C., Ellingson, E., et al. 1997, ApJL, 485, L13
Chiu, I., Mohr, J., McDonald, M., et al. 2016, MNRAS, 455, 258
Croston, J. H., Pratt, G. W., Böhringer, H., et al. 2008, A&A, 487, 431
de Haan, T., Benson, B. A., Bleem, L. E., et al. 2016, ApJ, 832, 95
Eisenhardt, P. R. M., Brodwin, M., Gonzalez, A. H., et al. 2008, ApJ, 684, 905
Fabian, A. C. 1994, ARA&A, 32, 277
Fabian, A. C. 2012, ARA&A, 50, 455
Fabian, A. C., Sanders, J. S., Allen, S. W., et al. 2003, MNRAS, 344, L43
Fakhouri, O., & Ma, C. 2010, MNRAS, 401, 2245
Fakhouri, O., Ma, C.-P., & Boylan-Kolchin, M. 2010, MNRAS, 406, 2267
Fassbender, R., Böhringer, H., Nastasi, A., et al. 2011, NJPh, 13, 125014
Gaspari, M., Brighenti, F., Temi, P., & Ettori, S. 2014, ApJL, 783, L10
Gaspari, M., Melioli, C., Brighenti, F., & D'Ercole, A. 2011, MNRAS, 411, 349
Gaspari, M., Temi, P., & Brighenti, F. 2017, MNRAS, 466, 677
Hasselfield, M., Hilton, M., Marriage, T. A., et al. 2013, JCAP, 7, 008
Hilton, M., Lloyd-Davies, E., Stanford, S. A., et al. 2010, ApJ, 718, 133
Hlavacek-Larrondo, J., McDonald, M., Benson, B. A., et al. 2015, ApJ, 805, 35
Hudson, D. S., Mittal, R., Reiprich, T. H., et al. 2010, A&A, 513, A37
Kravtsov, A. V., & Borgani, S. 2012, ARA&A, 50, 353
Madau, P., & Dickinson, M. 2014, ARA&A, 52, 415
Mantz, A., Allen, S. W., Rapetti, D., & Ebeling, H. 2010, MNRAS, 406, 1759
Mantz, A. B., Allen, S. W., Morris, R. G., et al. 2015, MNRAS, 449, 199
Mantz, A. B., Allen, S. W., Morris, R. G., & Schmidt, R. W. 2016, MNRAS, 456, 4020
Markevitch, M., Gonzalez, A. H., David, L., et al. 2002, ApJL, 567, L27
Marriage, T. A., Acquaviva, V., Ade, P. A. R., et al. 2011, ApJ, 737, 61
McBride, J., Fakhouri, O., & Ma, C.-P. 2009, MNRAS, 398, 1858
McDonald, M., Bayliss, M., Benson, B. A., et al. 2012, Natur, 488, 349
McDonald, M., Benson, B. A., Vikhlinin, A., et al. 2013, ApJ, 774, 23
McDonald, M., Benson, B. A., Vikhlinin, A., et al. 2014, ApJ, 794, 67
McDonald, M., Bulbul, E., de Haan, T., et al. 2016, ApJ, 826, 124
McNamara, B. R., & Nulsen, P. E. J. 2012, NJPh, 14, 055023
Medezinski, E., Battaglia, N., Coupon, J., et al. 2017, ApJ, 836, 54
Mohr, J. J., Evrard, A. E., Fabricant, D. G., & Geller, M. J. 1995, ApJ, 447, 8
Muzzin, A., Wilson, G., Yee, H. K. C., et al. 2009, ApJ, 698, 1934
Niemack, M. D., Ade, P. A. R., Aguirre, J., et al. 2010, Proc. SPIE, 7741, 77411S
Nurgaliev, D., McDonald, M., Benson, B. A., et al. 2013, ApJ, 779, 112
Nurgaliev, D., McDonald, M., Benson, B. A., et al. 2017, ApJ, 841, 5
Planck Collaboration, Ade, P. A. R., Aghanim, N., et al. 2011, A&A, 536, A8
Planck Collaboration, Ade, P. A. R., Aghanim, N., et al. 2014, A&A, 571, A29
Planck Collaboration, Ade, P. A. R., Aghanim, N., et al. 2015, A&A, 581, A14
Prasad, D., Sharma, P., & Babul, A. 2015, ApJ, 811, 108
Prasad, D., Sharma, P., & Babul, A. 2016, arXiv:1611.02710
Pratt, G. W., Croston, J. H., Arnaud, M., & Böhringer, H. 2009, A&A, 498, 361
Rafferty, D. A., McNamara, B. R., & Nulsen, P. E. J. 2008, ApJ, 687, 899
Reichardt, C. L., Stalder, B., Bleem, L. E., et al. 2013, ApJ, 763, 127
Rettura, A., Martinez-Manso, J., Stern, D., et al. 2014, ApJ, 797, 109
Santos, J. S., Rosati, P., Tozzi, P., et al. 2008, A&A, 483, 35
Santos, J. S., Tozzi, P., Rosati, P., & Böhringer, H. 2010, A&A, 521, 64
Sarazin, C. L. 2002, in Merging Processes in Galaxy Clusters, Vol. 272, ed. L. Feretti, I. M. Gioia, & G. Giovannini (Dordrecht: Kluwer), 1
Schuecker, P., Böhringer, H., Reiprich, T. H., & Feretti, L. 2001, A&A, 378, 408
Semler, D. R., Šuhada, R., Aird, K. A., et al. 2012, ApJ, 761, 183
Sifón, C., Battaglia, N., Hasselfield, M., et al. 2016, MNRAS, 461, 248
Stalder, B., Ruel, J., Šuhada, R., et al. 2013, ApJ, 763, 93
Stanford, S. A., Gonzalez, A. H., Brodwin, M., et al. 2014, ApJS, 213, 25
Staniszewski, Z., Ade, P. A. R., Aird, K. A., et al. 2009, ApJ, 701, 32
Sunyaev, R. A., & Zeldovich, Y. B. 1972, CoASP, 4, 173
Tozzi, P., Santos, J. S., Jee, M. J., et al. 2015, ApJ, 799, 93
Tremblay, G. R., Oonk, J. B. R., Combes, F., et al. 2016, Natur, 534, 218
Vanderlinde, K., Crawford, T. M., de Haan, T., et al. 2010, ApJ, 722, 1180
Vikhlinin, A., Burenin, R., Forman, W. R., et al. 2007, in Heating versus Cooling in Galaxies and Clusters of Galaxies, ed. H. Böhringer et al. (Berlin: Springer), 48
Vikhlinin, A., Burenin, R. A., Ebeling, H., et al. 2009, ApJ, 692, 1033
Vikhlinin, A., Kravtsov, A., Forman, W., et al. 2006, ApJ, 640, 691
Vikhlinin, A., McNamara, B. R., Forman, W., et al. 1998, ApJL, 498, L21
Voevodkin, A., & Vikhlinin, A. 2004, ApJ, 601, 610
Voit, G. M., Donahue, M., Bryan, G. L., & McDonald, M. 2015, Natur, 519, 203
Weißmann, A., Böhringer, H., Šuhada, R., & Ameglio, S. 2013, A&A, 549, A19
Wolf, C., Wisotzki, L., Borch, A., et al. 2003, A&A, 408, 499